A JANUARY SIMULATION EXPERIMENT WITH THE TWO-LAYER VERSION OF THE NCAR GLOBAL CIRCULATION MODEL

WARREN M. WASHINGTON and AKIRA KASAHARA

National Center for Atmospheric Research,[1] Boulder, Colo.

ABSTRACT

Results of a January simulation experiment with the two-layer version of the NCAR global circulation model are discussed. The model includes a hydrological cycle, horizontal and vertical turbulent transports of momentum, heat, and water vapor from the lower boundary and within the atmosphere, and calculations of solar and terrestrial radiation. Although the water vapor field interacts with the radiation calculations, the cloud distribution is a function of latitude and season. In this version of the model, the earth's orography is omitted as well as an explicit calculation of the surface temperature.

This version of the model has a spherical horizontal mesh spacing of 5° in both longitude and latitude and two vertical layers at 6-km height increments. The details of the finite-difference scheme for the model are presented.

The initial conditions for this experiment are based on an isothermal atmosphere at rest. The zonal mean cloudiness, the mean sea level temperature distribution, and the sun's declination are specified for January. The early stage of the numerical integration is characterized by a Hadley-type direct circulation due to the thermal contrasts between the continents and oceans. Within 2 weeks, the Hadley circulation breaks down due to baroclinic instability. This results in the typical three-cell meridional circulation. The comparison between computed and observed January climatology is discussed together with the presentation of momentum, moisture, and energy budgets. The main result from these budget calculations is that the Hadley cell is of dominant importance in the transport of various quantities within the Tropics and that baroclinic eddies are important in midlatitudes.

1. INTRODUCTION

In this article, we shall describe simulation results obtained from a two-layer version of the National Center for Atmospheric Research (NCAR) general circulation model. In a previous paper by Kasahara and Washington (1967), which will be referred to as paper I, the basic model equations were derived, together with the formulations of the heating/cooling and frictional processes. Also included in paper I is an historical review of other general circulation models and a discussion of the differences between these models and the NCAR model. We have modified several aspects of the model since paper I was published. A major modification is the addition of a complete hydrological cycle that allows for evaporation from the earth's surface, vertical and horizontal transport of moisture, and precipitation. The effect of orography has been added to the NCAR model but will not be discussed in this article. Some preliminary results with orography have been discussed by Kasahara and Washington (1969). For the radiation calculation, we have included the seasonal effect of cloudiness in which the total cloud amount is constant with time and is only a function of latitude.

After the introduction, the remaining portion of the article is arranged in the following manner. Section 2 briefly reviews the model equations. We introduce the equations used in the hydrological cycle in section 3. Sections 4 and 5 discuss the vertical/horizontal grid structure and finite-difference formulation. Also included in this section are the numerical approximations used for

the frictional and heating/cooling terms. The initial and boundary conditions used for this experiment are discussed in section 6. We have chosen to limit this article to a simulation of the January climatology without orography. The comparison between computed and observed January climatology is shown in section 7. The remaining sections 8 to 12 discuss, in the following order, angular momentum balance, moisture balance, zonal distribution of heating/cooling rates, energy balance, and conclusions.

2. MODEL EQUATIONS

In paper I, we derived the basic model equations and described the physical processes. Since the publication of that article, the major modification to our model has been the inclusion of a complete hydrological cycle. The basic equations that are actually used are listed along with the modifications.

The prognostic equations are the longitudinal and meridional equations of motion

$$\frac{\partial(\rho u)}{\partial t} = -\nabla\cdot(\rho u\mathbf{V}) - \frac{\partial}{\partial z}(\rho uw) - \frac{1}{a\cos\phi}\frac{\partial p}{\partial\lambda} + \left(f + \frac{u}{a}\tan\phi\right)\rho v + F_\lambda, \quad (1)$$

$$\frac{\partial(\rho v)}{\partial t} = -\nabla\cdot(\rho v\mathbf{V}) - \frac{\partial}{\partial z}(\rho vw) - \frac{1}{a}\frac{\partial p}{\partial\phi} - \left(f + \frac{u}{a}\tan\phi\right)\rho u + F_\phi, \quad (2)$$

---

and the pressure tendency equation

$$\frac{\partial p}{\partial t} = B + g\rho w - g \int_z^{z_T} \nabla \cdot (\rho \mathbb{V}) dz \qquad (3)$$

where z_T is the top of the model atmosphere, $B = \partial p / \partial t$ at $z = z_T$, and for a scalar quantity A,

$$\nabla \cdot A\mathbb{V} = \frac{1}{a \cos \phi} \left[\frac{\partial (Au)}{\partial \lambda} + \frac{\partial}{\partial \phi} (Av \cos \phi) \right]. \qquad (4)$$

The diagnostic equations are the hydrostatic equation

$$\rho = -\frac{1}{g} \frac{\partial p}{\partial z}, \qquad (5)$$

the Richardson equation

$$w = -\int_0^z \nabla \cdot \mathbb{V} dz - \frac{1}{\gamma} \int_0^z \frac{1}{p} (B+J) dz + \frac{1}{c_p} \int_0^z \frac{Q}{T} dz, \qquad (6)$$

and the equation for pressure change B at $z = z_T$ where $w = 0$:

$$B = \frac{\frac{1}{\gamma} \int_0^{z_T} \frac{J}{p} dz - \frac{1}{c_p} \int_0^{z_T} \frac{Q}{T} dz + \int_0^{z_T} \nabla \cdot \mathbb{V} dz}{-\frac{1}{\gamma} \int_0^{z_T} \frac{dz}{p}} \qquad (7)$$

where

$$J = \mathbb{V} \cdot \nabla p - g \int_z^{z_T} \nabla \cdot (\rho \mathbb{V}) dz. \qquad (8)$$

Temperature is computed from

$$T = -\frac{g}{R \frac{\partial}{\partial z} (\ln p)}. \qquad (9)$$

The longitudinal and meridional components of frictional force are

$$F_\lambda = \frac{\partial \tau_\lambda}{\partial z} + (F_\lambda)_H, \qquad (10a)$$

$$(F_\lambda)_H = \frac{1}{a \cos \phi} \frac{\partial}{\partial \lambda} (\rho K_{MH} D_T) + \frac{1}{a} \frac{\partial}{\partial \phi} (\rho K_{MH} D_S), \qquad (10b)$$

$$F_\phi = \frac{\partial \tau_\phi}{\partial z} + (F_\phi)_H, \qquad (11a)$$

and

$$(F_\phi)_H = \frac{1}{a \cos \phi} \frac{\partial}{\partial \lambda} (\rho K_{MH} D_S) - \frac{1}{a} \frac{\partial}{\partial \phi} (\rho K_{MH} D_T) \qquad (11b)$$

where

$$D_T = \frac{1}{a \cos \phi} \left[\frac{\partial u}{\partial \lambda} - \frac{\partial}{\partial \phi} (v \cos \phi) \right], \qquad (12)$$

$$D_S = \frac{1}{a \cos \phi} \left[\frac{\partial v}{\partial \lambda} + \frac{\partial}{\partial \phi} (u \cos \phi) \right], \qquad (13)$$

$$\tau_\lambda = \rho K_{MV} \frac{\partial u}{\partial z},$$

and $\qquad (14)$

$$\tau_\phi = \rho K_{MV} \frac{\partial v}{\partial z}.$$

Here, K_{MH} and K_{MV} are the horizontal and vertical kinematic eddy viscosity, respectively.

According to Smagorinsky (1963), we assume

$$K_{MH} = 2k_0^2 l^2 D \qquad (15)$$

where

$$D = \sqrt{D_T^2 + D_S^2} \qquad (16)$$

and k_0 is a proportionality constant which we have chosen to be 0.4. For the horizontal mesh size l, we assumed

$$l = a\Delta\lambda \cos \phi. \qquad (17)$$

The vertical and horizontal diffusion of sensible heat are given by

$$Q_d = -\frac{1}{\rho} \frac{\partial h}{\partial z} + \frac{c_p}{\rho a^2 \cos \phi} \left[\frac{1}{\cos \phi} \frac{\partial}{\partial \lambda} \left(\rho K_{TH} \frac{\partial \theta}{\partial \lambda} \right) + \frac{\partial}{\partial \phi} \left(\rho K_{TH} \cos \phi \frac{\partial \theta}{\partial \phi} \right) \right] \qquad (18)$$

where K_{TH} is the horizontal kinematic eddy viscosity (we assume in this paper that $K_{TH} = K_{MH}$), h is the vertical flux of sensible heat

$$h = -\rho c_p K_{TV} \left(\frac{\partial \theta}{\partial z} - \gamma_{CG} \right), \qquad (19)$$

θ is the potential temperature ($\theta = T(p_0/p)^{R/c_p}$; $p_0 = 1000$ mb), and γ_{CG} is a countergradient which is estimated by Deardorff (1966) as 0.65×10^{-5} Cc m^{-1} in the lower troposphere under clear sky conditions. For cloudy sky conditions, we would expect γ_{CG} to approach the value of the moist adiabat which is near 5×10^{-5} C cm^{-1}. We found experimentally a value of 5×10^{-5} C cm^{-1} at $z = z_s$ (z_s is the height of the surface boundary layer, of the order of 50 m), and 10^{-5} C cm^{-1} at 6 km gave reasonable results. If we use a value of 5×10^{-5} C cm^{-1} at 6 km, the atmosphere becomes too stable and, as a result, baroclinic waves weaken. On the other hand, if the value of γ_{CG} at $z = z_s$ is 10^{-5} C cm^{-1}, then a very unstable lapse rate is required between the midpoint of the lowest tropospheric layer and the boundary layer to obtain upward sensible heat flux.

To allow for the effect of free convection in the atmosphere, we assume that the vertical kinematic thermal diffusivity, K_{TV}, is a function of stability, as suggested by Deardorff (1967). For the unstable case where $\partial \theta / \partial z \leq \gamma_{CG}$, we use

$$K_{TV} = A_1 + A_2 \left[1 - \exp \left\{ A_3 \left(\frac{\partial \theta}{\partial z} - \gamma_{CG} \right) \right\} \right] \qquad (20)$$

in which $A_1 = 6 \times 10^5$ cm^2 sec^{-1}, $A_2 = 10^6$ cm^2 sec^{-1}, and $A_3 = 1.2 \times 10^5$ C^{-1} cm. For the stable case where $\partial \theta / \partial z > \gamma_{CG}$, we use

$$K_{TV} = \frac{A_1}{1 + A_4 R_i} \qquad (21)$$

where $A_4 = 40$. As minimum of K_{TV}, we assumed that for the layer just above the surface boundary layer K_{TV}

minimum$=5\times10^4$ cm^2 sec^{-1} and for the upper layer K_{TV} minimum$=10^3$ cm^2 sec^{-1}. The Richardson number, R_i, is defined by

$$R_i=\frac{g}{T}\left(\frac{\partial\theta}{\partial z}-\gamma_{CG}\right)\Big/\left[\left(\frac{\partial u}{\partial z}\right)^2+\left(\frac{\partial v}{\partial z}\right)^2\right].\qquad(22)$$

Equations (20) and (21) give a relatively large value of K_{TV} when the atmosphere is unstable and a relatively small value when the atmosphere is stable. $K_{MV}=K_{TV}$ is assumed throughout this paper even though there is some observational evidence that the magnitude of K_{TV} should be larger than that of K_{MV} in the unstable cases (for example, Lumley and Panofsky 1964).

The method of calculating radiative heating and cooling rates is discussed by Sasamori (1968a, 1968b).

It is customary to perform an adjustment in the vertical distribution of temperature to prevent the occurrence of gravitational instability. In the present calculations, we adopted the following two constraints on the vertical temperature distribution:

1) The total internal energy between two adjacent layers per unit area is conserved under such an adjustment, that is,

$$\int_0^{z_T}\rho T dz=\text{constant}\qquad(23)$$

where the density was assumed constant throughout the adjustment.

2) If the temperature lapse rate exceeds either the moist or dry adiabatic lapse rates, depending upon whether the vertical motion is upward or downward, respectively, we set

$$\frac{\partial T}{\partial z}=-\gamma_d\qquad\text{if }w<0\qquad(24)$$

and

$$\frac{\partial T}{\partial z}=-\gamma_m\qquad\text{if }w>0\qquad(25)$$

where γ_d and γ_m denote the dry and moist adiabatic lapse rates. Similar convective adjustments are used in Smagorinsky et al. (1965), Manabe et al. (1965), and Mintz (1965). In our scheme, the mean internal energy of the column is unchanged during adjustment; therefore, the amount of released latent heat added to the air is known as an explicit value of heating rate applied to the thermodynamic energy equation.

3. HYDROLOGICAL CYCLE

One of the most important heat sources in the earth's atmosphere is the latent heat released by condensation within clouds. Of course, not all of this heat energy is available to the atmosphere since many clouds evaporate, giving the atmosphere no net gain of heat. If, however, water droplets or ice particles actually fall out of the clouds without evaporation, the atmosphere will receive a net gain of heat. The formulation of the hydrological cycle in our experiments is based on a simple prescription of a complicated cloud physics process.

Let the specific humidity q be defined by

$$q=\frac{\epsilon e}{p-(1-\epsilon)e}\qquad(26)$$

where e is the partial pressure of water vapor and ϵ is the ratio of the molecular weight of water vapor to dry air ($\epsilon=0.622$). If air is saturated either over water or ice, it is designated by e_a, the saturation vapor pressure. The saturation specific humidity is

$$q_a=\frac{\epsilon e_a}{p-(1-\epsilon)e_a}.\qquad(27)$$

If the value of q exceeds that of q_a, the excess amount of water vapor is available for condensation in the form of liquid water. When the water vapor changes to liquid water, the latent heat of condensation is supplied to the air.

The specific humidity is also defined as

$$q=\frac{\rho_w}{\rho}\qquad(28)$$

where ρ_w is the density of water vapor and ρ is the density of air. Since the air carries the water vapor along with it, the velocity of the water vapor is the same as that of the air. Therefore, we have an equation of continuity of mass of water vapor similar in form to the equation of mass continuity, except that ρq replaces ρ and that condensation and diffusion of moisture come in:

$$\frac{\partial(\rho q)}{\partial t}=-\nabla\cdot(\rho q\mathbf{V})-\frac{\partial}{\partial z}(\rho q w)+M+\rho E,\qquad(29)$$

where M is the rate of condensation of water vapor per unit volume and E is the rate of change of water vapor content per unit mass due to the vertical and horizontal diffusion of water vapor.

If we assume that the condensed water remains in the same airmass as clouds, then we must set up two more equations dealing with the time rate of change of liquid water content and ice content. To simplify the problem, we assume that all the condensed water falls immediately out of the airmass in the form of precipitation. Since the condensation plays the role of a moisture sink, the only source comes from the term E in equation (29), which may be expressed in analogous form to momentum and sensible heat as

$$E=-\frac{1}{\rho}\frac{\partial r}{\partial z}+E_H\qquad(30)$$

where r denotes the vertical flux of water vapor. In the Ekman layer, r may be expressed as

$$r=-\rho K_{wv}\frac{\partial q}{\partial z}\qquad(31)$$

where K_{wv} denotes the vertical diffusivity of water vapor. In the surface boundary layer, r may be expressed as

$$r=-\rho C_{Dw}V_s(q_s-q_g)\qquad(32)$$

where q_s is the value of q at $z=z_s$, q_g is the saturation value of q at the earth's surface, and $C_{Dw}=0.7$ C_D. An empirical factor 0.7 was assumed to reduce the evaporation rate.

At the interface $(z=z_s)$ of the Ekman and Prandtl layers, we assume the condition

$$K_{wv}\frac{\partial q}{\partial z}=C_{Dw}V_s(q_s-q_g);\tag{33}$$

and at the upper boundary, we assume that

$$r=0 \quad \text{at } z=z_T.\tag{34}$$

In equation (30), the term E_H is defined analogously to momentum and sensible heat as

$$E_H=\frac{1}{\rho a^2 \cos \phi}\left[\frac{1}{\cos \phi}\frac{\partial}{\partial \lambda}\left(\rho K_{wH}\frac{\partial q}{\partial \lambda}\right)+\frac{\partial}{\partial \phi}\left(\rho K_{wH}\cos \phi\frac{\partial q}{\partial \phi}\right)\right]\tag{35}$$

where K_{wH} is the horizontal diffusivity of water vapor. We assume that K_{wH} and K_{wv} used in equations (35) and (31) have the same value as their counterparts for momentum and sensible heat.

We first forecast ρq by the use of equation (29), ignoring the term M. In this way, the ρq field at $t=t_0+\Delta t$ can be predicted from the space distribution of ρq at $t=t_0$ and $t=t_0-\Delta t$. From the dynamical prediction equations, we can also find the density of air ρ and the temperature T at $t=t_0+\Delta t$. Therefore, we can compute the saturation specific humidity q_a.

Now at $t=t_0+\Delta t$, we compute

$$(\rho q)_{t_0+\Delta t}-\beta(\rho q_a)_{t_0+\Delta t}\equiv M\Delta t\tag{36}$$

where β is a relative humidity factor of 95 percent. If $M\Delta t<0$, the air is unsaturated, and the initial guess that $M=0$ at $t=t_0$ is correct. If $M\Delta t>0$, we assume that condensation occurs and the condensed water falls out of the system as precipitation. Condensation of water $M\Delta t$ then releases the latent heat of water vapor, and the heating rate is given by

$$\rho Q_c=LM\tag{37}$$

where L is the latent heat of condensation. We have placed an additional constraint upon the supersaturated air which is that the motion be upward (that is, $w>0$). Ogura and Charney (1962) have used such a restriction in a squall line model.

4. VERTICAL AND HORIZONTAL GRID STRUCTURE

The vertical grid structure was so chosen that the winds, temperatures, specific humidities, densities, and heating rates are representative of layers; whereas the pressures, vertical velocities, and vertical fluxes are either computed
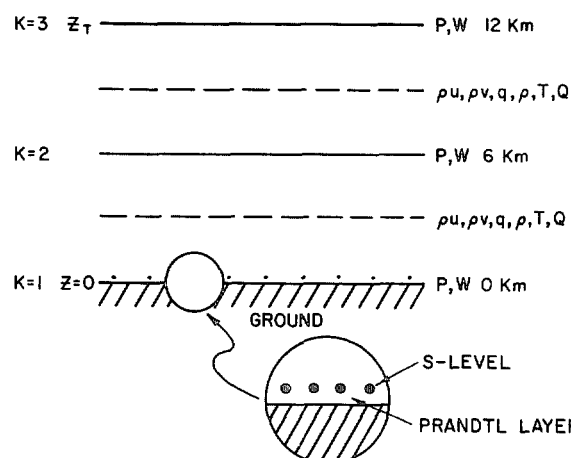

FIGURE 1.—Vertical grid structure for the two-layer model.

or specified at the top and bottom of these layers. Figure 1 shows the placement of the variables. The solid horizontal lines show the ground level $z=0$ and the levels at $z=\Delta z$ and $2\Delta z$. The height increment Δz is chosen to be 6 km in the two-layer model. The top level is located at $z=z_T$ $(=2\Delta z)$ which corresponds approximately to the 200-mb level. They are called integer levels in terms of the index k as shown. The pressure p and vertical velocity w are placed on these levels. The dashed lines denote the levels located at the height of $(1/2)\Delta z$ and $(3/2)\Delta z$. They are called half-integer levels. The momenta ρu and ρv, the specific humidity q, the density ρ, the temperature T, and the heating rate Q are placed on these levels. The top of the Prandtl layer is denoted by subscript s, and the ground level is denoted by subscript g. Since the height of the anemometer level is very small compared with Δz, the level $k=1$ is virtually identical to the s level in height.

The horizontal grid points are placed at longitude and latitude intersections of 5° increments. However, the grid system is staggered in time, as shown in figure 2. The cross and dot points in figure 2 are at different time levels of one time increment, Δt, apart. The finite-difference formulation uses the space-centered approximation. Thus, the use of the staggered scheme leads to a saving of one-half the computing time.

Near the Poles, equal increments of longitude result in the reduction of geographical distances in the longitude because of the convergence of the meridians. The reduction of geographical distances between grid points near the Poles imposes a stringent restriction on the selection of a time increment for solving the equations by an explicit method. To avoid this difficulty, we have skipped grid points near the Poles, as shown in figure 2. At both 75° and 80° north and south, the number of grid points along a latitude is reduced to half. Finally, at 85° north and south, the number of grid points is again halved. Values at the missing points, when needed, are filled in by linear interpolation at the same time level along the same latitude circle. A similar skipping method near the Poles
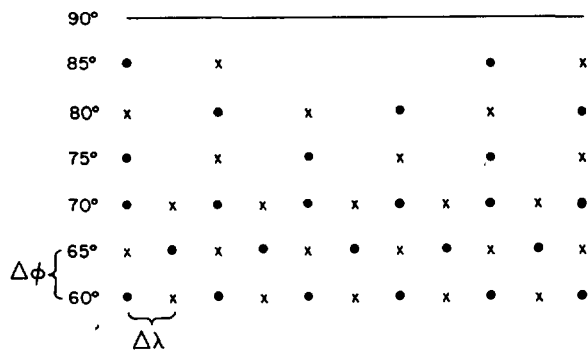
FIGURE 2.—Portion of the horizontal grid structure showing where points are skipped near the Pole.

has been devised by Leith (1965) in connection with the use of spherical coordinates.

The Poles are singular points for the definition of momenta. However, the values of momenta at the Poles are never used, as discussed in the next section. Pressure is the only variable that is required for the calculations at the Poles. We use arithmetic averaging of the values of pressure at 85° north or south as the respective Pole values. This method leads to the generation of small-scale disturbances near the Poles and, perhaps, weakening of meridional motions near the Poles. Nevertheless, this treatment appears to be stable computationally.

5. FINITE-DIFFERENCE EQUATIONS

The finite-difference method applied to the horizontal momentum equations (1) and (2) is based upon a scheme that was originally proposed by Lax and Wendroff (1960) and later modified by Richtmyer (1963). We have since further modified this method to have much less damping of the solution as described later in this section. Richtmyer's scheme is termed the *two-step Lax-Wendroff method* in which the first step is called "diffusing" and the second step is called "leapfrog." This scheme was developed to handle equations written in divergence form and does not prescribe uniquely the treatment of Coriolis and diffusion terms in the atmospheric equations. Houghton et al. (1966) investigated this question and discussed the computational stability of finite-difference schemes based on the two-step Lax-Wendroff method which are applied to the barotropic primitive equations, including Coriolis and diffusion terms.

To explain how the two-step Lax-Wendroff scheme is used here, let us consider the following simple partial differential equation as an example:

$$\frac{\partial u}{\partial t} = \frac{\partial F(u)}{\partial x} \tag{38}$$

where x and t denote the space and time coordinates, respectively. To write the difference equations, we shall use a rectangular net in the x-t plane, with spacings Δx

and Δt. We abbreviate any function $S(x,t)$ of $x=j\Delta x$ and $t=n\Delta t$ as S_j^n where n and j are integers. The two-step Lax-Wendroff method applied to equation (38) may be written as the combination of the following two schemes which are used for alternate time cycles:

$$u_j^{n+1} = \frac{1}{2}(u_{j+1}^n + u_{j-1}^n) + \frac{\Delta t}{2\Delta x}(F_{j+1}^n - F_{j-1}^n) \tag{39a}$$

and

$$u_j^{n+2} = u_j^n + \frac{\Delta t}{\Delta x}(F_{j+1}^{n+1} - F_{j-1}^{n+1}). \tag{39b}$$

Step (39b) is a centered (in time and space) scheme often called the leapfrog scheme. Step (39a) is labeled the diffusing scheme. The diffusing scheme has a built-in smoothing effect that damps short-wave disturbances.

To see the effect of smoothing, let us point out that the diffusing step (39a) can be rewritten in the following form

$$u_j^{n+1} = u_j^{n-1} + \frac{\Delta t}{\Delta x}(F_{j+1}^n - F_{j-1}^n) + (u_{j+1}^n + u_{j-1}^n - u_j^{n-1} - u_j^{n+1}). \tag{40}$$

If we ignore the last four quantities in parentheses, the scheme is identical to the leapfrog scheme (39b), except that the formula is applied at the time step n instead of $n+1$. The remainder of (40) is a diffusion term of the DuFort and Frankel type (1953) in which the diffusivity is set equal to $(\Delta x)^2/\Delta t$. This means that the so-called diffusing scheme (39a) is identical to the combination of the leapfrog scheme and the diffusion term. Because of the presence of this artificial smoothing, the two-step Lax-Wendroff scheme is suited for numerical solutions of *nonlinear* hyperbolic partial differential equations. The principal difference in the method used here and in those discussed above is that the diffusing step is applied less often so as not to overdamp short waves. By experimentation, it was found sufficient to apply the diffusing step only after every 135 steps of leapfrog.

To express the finite-difference equations used in the actual calculations, let us introduce the following operators applied at the grid point (i, j, k):

$$\delta_\lambda(\ ) \equiv \{(\ )_{i+1} - (\ )_{i-1}\}/2\Delta\lambda, \tag{41a}$$

$$\delta_\phi(\ ) \equiv \{(\ )_{j+1} - (\ )_{j-1}\}/2\Delta\phi, \tag{41b}$$

$$\delta_z(\ ) \equiv \{(\ )_{k+\frac{1}{2}} - (\ )_{k-\frac{1}{2}}\}/\Delta z, \tag{41c}$$

$$(\overline{\ })^\lambda \equiv \frac{1}{2}\{(\ )_{i+1} + (\ )_{i-1}\}, \tag{42a}$$

$$(\overline{\ })^\phi \equiv \frac{1}{2}\{(\ )_{j+1} + (\ )_{j-1}\}, \tag{42b}$$

$$(\overline{\ }) \equiv \frac{1}{2}\{(\overline{\ })^\lambda + (\overline{\ })^\phi\}, \text{ and} \tag{43a}$$

$$(\tilde{\ }) \equiv \frac{1}{2}\{(\ )_{k+\frac{1}{2}} + (\ )_{k-\frac{1}{2}}\}. \tag{43b}$$

The definitions (41a) and (42a) are modified near the Poles to allow for the skipping of grid points as described in section 4.

The finite-difference equations for (1) and (2), written at the grid point $(i,j,k+\frac{1}{2})$, are

$$\frac{\partial(\rho u)^n}{\partial t}=-\frac{1}{a\cos\phi}[\delta_\lambda(\rho u^2+\tilde{p})^n+\delta_\phi(\rho uv\cos\phi)^n]$$

$$-\delta_z(\overline{\tilde{\rho}uw})^n+\tfrac{1}{2}f^*\{(\rho v)^{n+1}+(\rho v)^{n-1}\}+F_\lambda^{n-\frac{1}{2}}\quad(44)$$

and

$$\frac{\partial(\rho v)^n}{\partial t}=-\frac{1}{a\cos\phi}[\delta_\lambda(\rho uv)^n+\delta_\phi(\rho v^2\cos\phi)^n]-\frac{1}{a}\delta_\phi(\tilde{p})^n$$

$$-\delta_z(\overline{\tilde{\rho}vw})^n-\tfrac{1}{2}f^*\{(\rho u)^{n+1}+(\rho u)^{n-1}\}+F_\phi^{n-\frac{1}{2}}\quad(45)$$

where

$$f^*=f+\frac{(\bar{u})^n}{a}\tan\phi.$$

The superscript n indicates the time level.

The time derivative term for the diffusing step is approximated by

$$\frac{\partial(A)^n}{\partial t}=\frac{(A)^{n+1}-(\overline{A})^n}{\Delta t},\quad(46)$$

where A stands for either ρu or ρv. For the leapfrog step, it is approximated by

$$\frac{\partial(A)^n}{\partial t}=\frac{(A)^{n+1}-(A)^{n-1}}{2\Delta t}.\quad(47)$$

Note that the Coriolis terms in equations (44) and (45) are evaluated by applying the average of two time levels. One is forward in time, and the other is lagged in time. The system of simultaneous equations for these quantities can be set up to solve for $(\rho u)^{n+1}$ and $(\rho v)^{n+1}$.

A finite-difference form of the horizontal diffusion term (10b) at $(i,j,k+\frac{1}{2})$ at time step n is

$$(F_\lambda)_H^{n-\frac{1}{2}}=\frac{1}{2a\cos\phi\,\Delta\lambda}\,[(\rho K_{MH}D_T)_{i+\frac{1}{2},j+\frac{1}{2}}$$

$$+(\rho K_{MH}D_T)_{i+\frac{1}{2},j-\frac{1}{2}}-(\rho K_{MH}D_T)_{i-\frac{1}{2},j+\frac{1}{2}}$$

$$-(\rho K_{MH}D_T)_{i-\frac{1}{2},j-\frac{1}{2}}]_{k+\frac{1}{2}}^{n-\frac{1}{2}}+\frac{1}{2a\Delta\phi}\,[(\rho K_{MH}D_s)_{i-\frac{1}{2},j+\frac{1}{2}}$$

$$+(\rho K_{MH}D_s)_{i+\frac{1}{2},j+\frac{1}{2}}-(\rho K_{MH}D_s)_{i-\frac{1}{2},j-\frac{1}{2}}$$

$$-(\rho K_{MH}D_s)_{i+\frac{1}{2},j-\frac{1}{2}}]_{k+\frac{1}{2}}^{n-\frac{1}{2}}\quad(48)$$

where, for example,

$$\rho_{i+\frac{1}{2},j+\frac{1}{2},k+\frac{1}{2}}^{n-\frac{1}{2}}=\tfrac{1}{4}(\rho_{i,j}^{n-1}+\rho_{i,j+1}^n+\rho_{i+1,j+1}^{n-1}+\rho_{i+1,j}^n)_{k+\frac{1}{2}},$$

$$K_{MH}^{n-\frac{1}{2}}|_{i+\frac{1}{2},j+,\frac{1}{2}k+\frac{1}{2}}=2k_0^2l^2D_{i+\frac{1}{2},j+\frac{1}{2},k+\frac{1}{2}}^{n-\frac{1}{2}}$$

$$=2k_0^2l^2(\sqrt{D_T^2+D_s^2})_{i+\frac{1}{2},j+\frac{1}{2},k+\frac{1}{2}}^{n-\frac{1}{2}},$$

and

$$D_T^{n-\frac{1}{2}}|_{i+\frac{1}{2},j+\frac{1}{2},k+\frac{1}{2}}=\frac{1}{a(\cos\phi_j+\cos\phi_{j+1})}\,[\{u_{i+1,j+1}^{n-1}+u_{i+1,j}^n$$

$$-u_{i,j+1}^n-u_{i,j}^{n-1}\}/\Delta\lambda-\{(v_{i,j+1}^n+v_{i+1,j+1}^{n-1})\cos\phi_{j+1}$$

$$-(v_{i,j}^{n-1}+v_{i+1,j}^n)\cos\phi_j\}/\Delta\phi]_{k+\frac{1}{2}}.$$

Similar expressions can be given to D_s, the other compo-

nents of equation (48), and the horizontal diffusion term for sensible heat and for water vapor. The vertical diffusion terms in (10a) and (11a) are calculated in a straightforward manner at the $n-1$ time level.

Next, we shall present a finite-difference form of the pressure tendency equation (3) written at (i,j,k). It is expressed by

$$\frac{\partial(p)^n}{\partial t}=B^n+g(\overline{\tilde{\rho}}w)^n-\frac{g\Delta z}{a\cos\phi}\sum_{l=k}^{K-1}[\delta_\lambda(\rho u)+\delta_\phi(\rho v\cos\phi)]_{l+\frac{1}{2}}^n$$

$$(49)$$

where $K=3$ for the two-layer model and

$$B^n=\frac{\partial(p)^n}{\partial t}\quad\text{at }z=z_T.\quad(50)$$

The pressure tendencies given by equations (49) and (50) are approximated by the leapfrog scheme (47). The continuous use of the leapfrog scheme for a long period eventually leads to the growth of a computational mode that is manifested by uncoupling of odd and even horizontal mesh points since these mesh points are staggered in time. These difficulties are avoided in the momentum equations by application of the diffusing step. However, when the diffusing step was applied once every 135 time steps to the pressure tendency calculations, it was found that the diffusing step still gave relatively strong damping in calculating the pressure tendencies. As pointed out in connection with equation (40), this diffusing step contains an artificial diffusion term in which the magnitude of the diffusivity is rather large. Thus to weaken the degree of smoothing that appeared in the diffusing step, we use the following nonlinear smoothing operation *to the odd or even meshes*, alternating between meshes every 45 time steps. The smoothing formula given at (i,j,k) is then

$$\mathcal{M}=\frac{3}{100|\delta p|_{max}}[|p_{i+1,j}^n-p_{i,j}^{n+1}|(p_{i+1,j}^n-p_{i,j}^{n+1})-|p_{i,j}^{n+1}$$

$$-p_{i-1,j}^n|(p_{i,j}^{n+1}-p_{i-1,j}^n)+|p_{i,j+1}^n-p_{i,j}^{n+1}|(p_{i,j+1}^n$$

$$-p_{i,j}^{n+1})-|p_{i,j}^{n+1}-p_{i,j-1}^n|(p_{i,j}^{n+1}-p_{i,j-1}^n)]\quad(51)$$

where the factor 3/100 was found by experimentation and $|\delta p|_{max}$ is the maximum absolute difference between p at a point (i,j,k) and p at the four immediately neighboring points in horizontal coordinates. Thus, the pressure at the grid point (i,j,k) is computed by

$$p^{n+1}=p^{n-1}+\frac{\partial(p)^n}{\partial t}2\Delta t\quad(52)$$

for 45 steps, and then one step using equation (52) followed by

$$p^{n+1}+\mathcal{M}\rightarrow p^{n+1}.\quad(53)$$

Then we repeat this cycle.

Now we shall describe the method of computation of the three *diagnostic variables* w, ρ, and T. For evaluating w using (6), it is necessary to compute the quantity J defined by equation (8) using a finite-difference method.

The following formulas are used to evaluate J_k, the quantity J at (i,j,k).

For $k=1$,

$$J_1 = \frac{1}{a \cos \phi} [\bar{u}_s^\lambda \delta_\lambda p_1 + \overline{(v_s \cos \phi)}^\phi \delta_\phi p_1]$$
$$- \frac{g \Delta z}{a \cos \phi} \sum_{l=1}^{K-1} [\delta_\lambda(\rho u) + \delta_\phi(\rho v \cos \phi)]_{l+\frac{1}{2}}. \quad (54)$$

For $1 < k < K$,

$$J_k = \frac{1}{a \cos \phi} [\bar{u}_k^\lambda \delta_\lambda p_k + \overline{(\tilde{v}_k \cos \phi)}^\phi \delta_\phi p_k]$$
$$- \frac{g \Delta z}{a \cos \phi} \sum_{l=k}^{K-1} [\delta_\lambda(\rho u) + \delta_\phi(\rho v \cos \phi)]_{l+\frac{1}{2}}. \quad (55)$$

For $k=K$,

$$J_K = \frac{1}{a \cos \phi} [\bar{u}_{K-\frac{1}{2}}^\lambda \delta_\lambda p_K + \overline{(v_{K-\frac{1}{2}} \cos \phi)}^\phi \delta_\phi p_K]. \quad (56)$$

The finite-difference version of equation (6) for w at (i,j,k,n) is

$$w_k^n = w_{k-1}^n - \sum_{l=1}^{k-1} \left[\frac{1}{a \cos \phi} \{ \delta_\lambda u + \delta_\phi(v \cos \phi) \}_{l+\frac{1}{2}}^n \right.$$
$$+ \frac{1}{(\gamma \bar{p}_{l+\frac{1}{2}})^n} \{ B^n + \frac{1}{2}(J_{l+1}^n + J_l^n) \}$$
$$\left. - \left(\frac{Q}{c_p T} \right)_{l+\frac{1}{2}} \right] \Delta z \quad \text{for } K > k > 1 \quad (57)$$

where Q is evaluated using quantities at n and $n-1$ time levels.

At $k=1$, $w=0$ is the lower boundary condition. At $k=K$, the quantity w also vanishes because of the upper boundary condition. Thus, we put $k=K$ in equation (57); then, the right-hand side of (57) becomes identical to zero. From this condition, the unknown quantity B^n can be evaluated as shown by equation (7).

Finally, the density $\rho_{k+\frac{1}{2}}$ and temperature $T_{k+\frac{1}{2}}$ are computed from equations (5) and (9) as follows:

$$\rho_{k+\frac{1}{2}} = -\delta_z p/g \quad (58)$$

and

$$T_{k+\frac{1}{2}} = \frac{g \Delta z}{R \ln(p_k/p_{k+1})}. \quad (59)$$

6. INITIAL AND BOUNDARY CONDITIONS

The lower and upper boundary conditions of the problem are described in section 3 of paper I. The value of the drag coefficient, C_D, is assumed to be 0.003. The surface wind speed, V_s, which enters into the Prandtl layer equations (3.2) of paper I gives reasonable results in regimes of relatively strong winds. However, in light winds and highly stable stratifications, the formula for the sensible heat flux in (3.2) of paper I may be unsatisfactory (Petterssen et al. 1962); therefore, to overcome the difficulty we have set a minimum V_s of 5 m sec^{-1}. The prescription for a minimum V_s is also needed for an experiment starting from the atmosphere of no horizontal motion, because

without this prescription the fluxes of heat and moisture are initially zero and remain too small for a great length of time.

The atmosphere is initially at rest, and the vertical pressure distribution is given for an isothermal atmosphere by

$$p_k = 1013.2 \exp\{-g(k-1)\Delta z/(RT^*)\} \text{mb} \quad (60)$$

where $k=1,2,3$ and T^* is a constant 240°K. We choose a slightly cold isothermal atmosphere rather than a warm one because warming by release of latent heat and vertical transport of sensible heat is faster than cooling by the relatively slow process of long-wave radiation starting from an atmosphere which is relatively warm.

The following external conditions of the model are prescribed for a simulated January climatology.

a) Mean sea level temperature distribution of the earth's surface shown in figure 3. The same boundary conditions are assumed for land and ocean areas.

b) Mean January zonal distribution of total cloudiness shown in figure 4. The data for the Northern Hemisphere were taken from Telegadas and London (1954), and for the Southern Hemisphere from Clapp (1964).

c) Sun's declination for mid-January (−21.2°).

Because of the north-south differential heating applied at day zero, horizontal pressure gradients immediately develop which in turn start motions. These initial motions show primarily the characteristic Hadley-type circulation in both hemispheres. However, because the surface temperature and incoming solar radiation are given for mid-January conditions, the primary ascending current is displaced south of the Equator into the Southern Hemisphere. This direct circulation is not entirely zonal since the nonzonal features of the sea-level temperature distribution are reflected in the atmospheric flow. After approximately 20 days, the north-south temperature gradients become supercritical with respect to baroclinic instability, and baroclinic waves begin to form. It is interesting to note that the first baroclinic waves in the Northern Hemisphere usually develop over the relatively warm ocean areas.

After the onset of baroclinic waves, the direct circulation breaks down. Long tongues of low pressure extend poleward between tongues of high pressure that extend equatorward in the surface pressure field. This pattern of alternating low and high pressures is tilted from northeast to southwest in the Northern Hemisphere and from northwest to southeast in the Southern Hemisphere. Eventually, these tongues form closed centers of Highs and Lows. The Highs moved equatorward while the Lows moved northward; finally, the characteristic three-cell meridional structure is formed.

7. COMPARISON BETWEEN OBSERVED AND COMPUTED CLIMATOLOGY

As pointed out by Lorenz (1967), we have a firm knowledge of the observed state of only certain quantities. These quantities are, for example, the zonal means of temperature, specific humidity, and the east-west com-

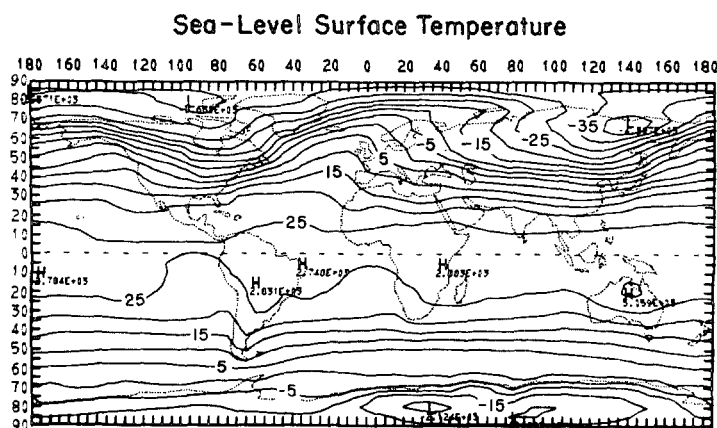Sea-Level Surface Temperature

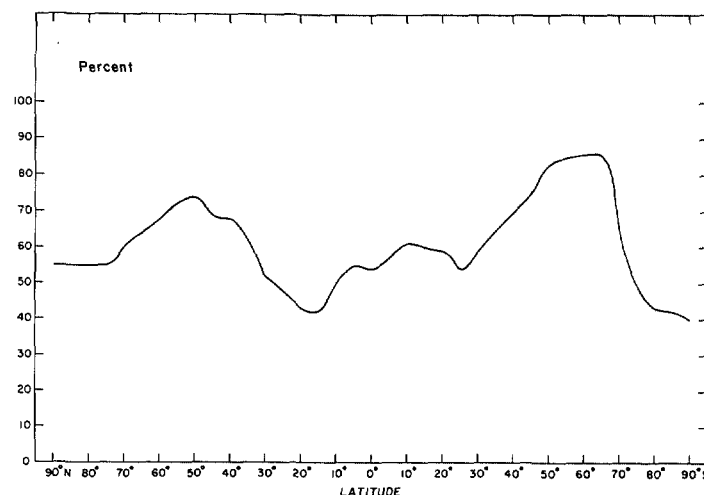FIGURE 3.—January mean sea level temperature distribution with 5°C contours.

FIGURE 4.—Zonal mean total cloudiness for January.

ponent of wind; whereas the zonal means of north-south and vertical components of wind are not observed with sufficient accuracy to have reliable statistics. We shall show in this section many sources of observed data to compare with the computed.

The zonal mean of the computed variables is averaged over a 60-day period from day 21 through day 80. These variables are compared with observed quantities at approximately the same levels used in the model. The computed zonal mean distributions of pressure at 0 (sea level), 6, and 12 km are shown in figure 5 together with a climatological zonal mean of pressure at the same levels. The sources for the observed data for the Southern Hemisphere are Taljaard et al. (1969); for the Northern Hemisphere, the sea-level data are from O'Conner (1961); and data at 6 and 12 km were obtained from Telegadas and London (1954).

The computed pressure distribution at 12 km agrees fairly well with the observed, although the computed value, on the average, is about 5 mb higher than the observed. This suggests that formula (7) used to compute $\partial p/\partial t$ at $z=z_T$ is working well. At the 6-km level, the computed pressure in the Tropics is satisfactory, but the computed pressure distribution fails to develop the strong gradient because the computed pressures at the two Poles are about 20 mb higher than the observed values. The tendency to produce higher pressure in the higher latitudes is most pronounced in the computed sea-level pressure distribution. Between 60° N. and 40° S., the computed sea-level pressure distribution agrees with the observed. However, in the higher latitudes, the computed pressure is higher than the observed by as much as 40 mb. The tendency to produce higher pressure near the Poles is also reported by Kurihara and Holloway (1967) in their computation of global circulation. Preliminary results based on our two-layer version incorporating the dynamic effects of the earth's orography show that the building up of high pressure near both Poles does not appear (Kasahara and Washington 1969). Results from the six-layer

model with a height increment of 3 km, without the earth's orography, do not show the buildup of high pressure near the Poles. It seems that the high pressure near the Poles in the present two-layer version is produced by insufficient meridional heat transport caused by truncation errors. Even in the two-layer version, the dynamic effect of orography appears to increase meridional heat transport in the high latitudes. Being a result of increased meridional heat transport, the buildup of high pressure in the high latitudes may be eliminated.

The observed and computed zonal mean temperature distributions are compared in figure 6. The observed data are taken from Palmén and Newton (1969) and Burdecki (1955). The computed temperature distribution agrees with the observed at the 3-km level, but the computed temperature at 9 km in the Tropics is higher than the observed by as much as 16°C. This discrepancy does not appear so large in the six-layer model; therefore, it is partly caused by the poor vertical resolution of the two-layer model.

The computed mean zonal wind, u, is shown in figure 7 with observed data from Buch (1954), Mintz (1954), Miyakoda (1963), Obasi (1963), Schwerdtfeger and Martin (1964), van Loon et al. (1970), and Wiin-Nielsen et al. (1964). The computed results consistently underestimate the wind speed, especially in the Southern Hemisphere. This underestimation is due partly to the poor vertical resolution of this version of the model. Preliminary results from the six-layer version show a much stronger zonal wind distribution. In the computation, weak tropical easterlies are present at the lower level but are not found at the upper level in the zonal average.

The zonal mean of computed meridional wind, v, is compared with the observed in figure 8. The sources for observed data are Gilman (1963), Holopainen (1967), Mintz and Lang (1955), Miyakoda (1963), Obasi (1963), Palmén et al. (1958), Palmén and Vuorela (1963), and Tucker (1959). The distributions of the computed zonal
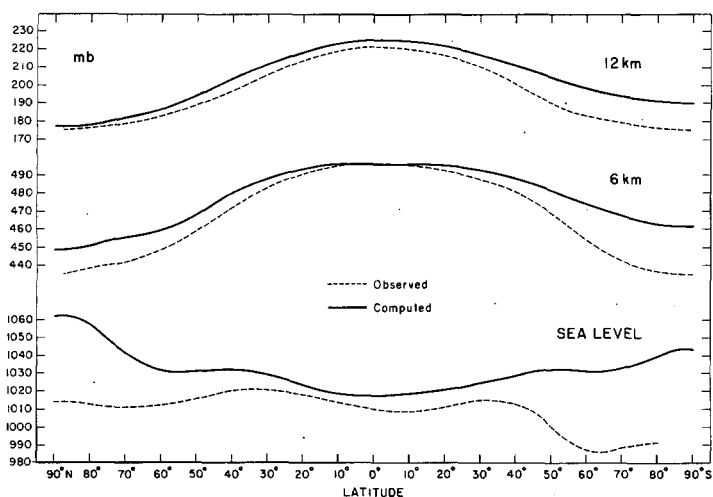
FIGURE 5.—Computed and observed January mean zonal pressures, at sea level, 6 km, and 12 km in millibars.
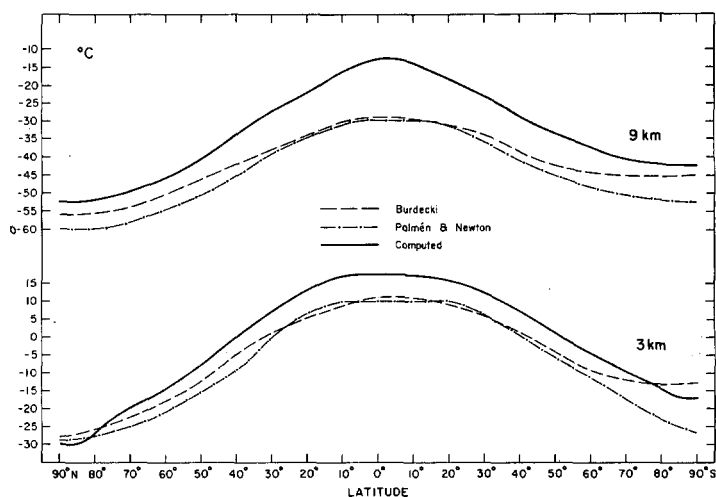

FIGURE 6.—Computed and observed January mean zonal temperature at 3 km and 9 km in °C.

mean of meridional wind at both levels fit reasonably well in the observed distributions which show rather large dispersions among themselves. Note that the computed maximum does appear to be too far south in comparison to the observed. The computed distributions in the Southern Hemisphere agree more nearly with the data of Gilman (1963), which are computed from momentum and mass balance considerations, rather than the data of Obasi (1963), which are computed by direct measurements. In direct measurements, there can be two sources of error. One is that the station data are mostly over land areas where local geographical effects may give biased local meridional winds; and, second, the smallness of the meridional wind requires accurate data. In balanced computations, these difficulties are likely to be reduced with knowledge of the other meteorological variables using the equations of motion and the equation of continuity.

Figure 9 shows the comparison between computed and observed vertical velocity. The sources for the observed data are Gilman (1963), Jensen (1961), Kidson et al. (1969), Mintz and Lang (1955), Miyakoda (1963), and Tucker (1959). Since these "observed" results are obtained indirectly from actual data, we can expect the accuracy to be based in part upon the method of derivation. Basically, the computed results show the expected Hadley circulation in the Tropics, where the main ascending branch is displaced below the Equator, and a weak indirect circulation in midlatitudes. There is also evidence of weak directly driven polar cells indicating the usual three-cell meridional structure.

The distribution of the zonal mean of specific humidity is shown in figure 10. Observed data were obtained from Peixoto and Crisi (1965) for the Northern Hemisphere and computed from data by van Loon et al. (1970) for the Southern Hemisphere. The computed value is almost twice as large as the observed at 3 km. This discrepancy
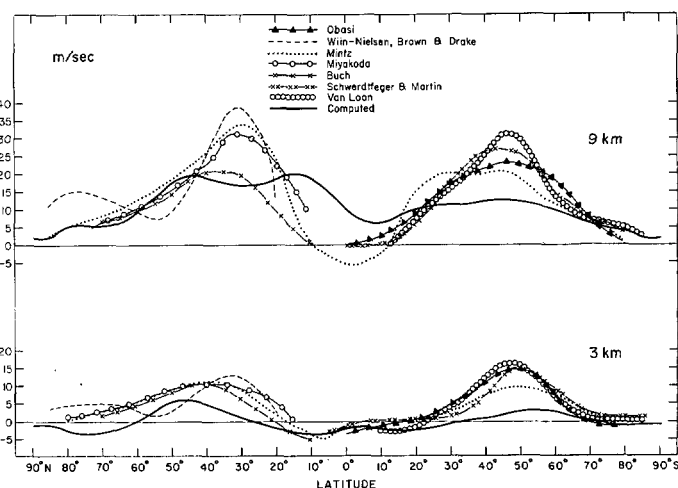
FIGURE 7.—Computed and observed January mean zonal wind u, at 3 km and 9 km in m sec^{-1}.

is due to the fact that the model atmosphere has a tendency to be saturated, whereas the observed zonal mean relative humidity at 3 km is in the range of 60 percent, according to Telegadas and London (1954). Part of this discrepancy is also attributed to the excessively warm tropical temperatures in this version of the model.

8. ANGULAR MOMENTUM

Let m denote the absolute angular momentum for a unit mass defined by

$$m = ua \cos \phi + a^2 \Omega \cos^2 \phi. \tag{61}$$

The first term is the angular momentum of motion relative to the earth's surface that we shall call u-angular momentum. The second term is the angular momentum due to the earth's rotation that we shall call Ω-angular momentum.
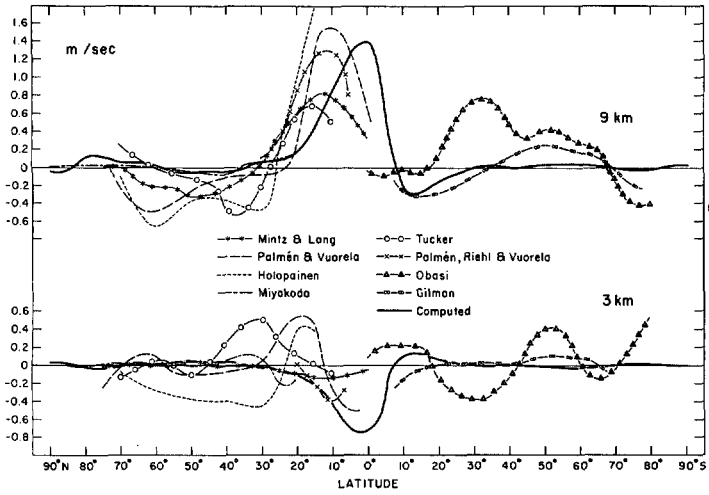
FIGURE 8.—Computed and observed January mean zonal meridional wind, v, at 3 km and 9 km in m sec^{-1}. Note that the Obasi data represent a seasonal average for the Southern Hemisphere summer.

FIGURE 9.—Computed and observed January mean zonal vertical velocity, w, in cm sec^{-1}.

Multiplying equation (1) by $a \cos \phi$, we obtain the angular momentum equation in the form

$$\frac{\partial}{\partial t}(\rho m) + \nabla \cdot (\rho m \mathbf{V}) + \frac{\partial}{\partial z}(\rho m w) = -\frac{\partial p}{\partial \lambda} + F_\lambda \, a \cos \phi. \quad (62)$$

For any variable A, we define the zonal mean operator, $\overline{A}$, given by

$$\overline{A} = \frac{1}{2\pi}\int_0^{2\pi} A \, d\lambda, \quad A = \overline{A} + A'', \quad \overline{A''} = 0 \quad (63)$$

and the density-weighted mean, $\hat{A}$, given by

$$\hat{A} = \overline{\rho A}/\overline{\rho}, \quad A = \hat{A} + A', \quad \overline{\rho A'} = 0. \quad (64)$$

Applying the zonal mean operator (63) to (62) and using (64), we find

$$\frac{\partial}{\partial t}(\overline{\rho}\hat{m}) = -\frac{1}{a\cos\phi}\frac{\partial}{\partial\phi}[(\overline{\rho}\hat{v}\hat{m} + \overline{\rho v'm'})\cos\phi]$$
$$- \frac{\partial}{\partial z}[\overline{\rho}\hat{w}\hat{m} + \overline{\rho w'm'}] + \overline{F_\lambda}\, a\cos\phi. \quad (65)$$

This is the zonally averaged equation of the absolute angular momentum per unit volume. Note that, by definition (61),

$$\overline{\rho}\hat{v}\hat{m} = \overline{\rho}\hat{v}\hat{u}\, a\cos\phi + \overline{\rho}\hat{v}\, a^2\Omega\cos^2\phi,$$

$$\overline{\rho v'm'} = \overline{\rho u'v'}\, a\cos\phi,$$

$$\overline{\rho}\hat{w}\hat{m} = \overline{\rho}\hat{w}\hat{u}\, a\cos\phi + \overline{\rho}\hat{w}\, a^2\Omega\cos^2\phi,$$

and $\qquad\qquad\qquad\qquad\qquad\qquad\qquad\qquad (66)$

$$\overline{\rho w'm'} = \overline{\rho w'u'}\, a\cos\phi.$$

With reference to (10a), the frictional term $\overline{F_\lambda}$ is defined as

$$\overline{F_\lambda} = \frac{\overline{\partial\tau_\lambda}}{\partial z} + (\overline{F_\lambda})_H. \quad (67)$$

Figure 11 shows the global averages of the absolute angular momentum $\overline{\rho}\hat{m}$ at the upper and lower levels which are plotted as functions of time. In the earlier part of the calculation, the value at each level changed rapidly due to the change in density caused by the vertical redistribution of mass from the initial isothermal state. Therefore, in the following study of statistics, we took a 60-day period from day 21 to day 80 avoiding the earlier stage of atmospheric adjustment.

Figure 12 shows the latitudinal distributions of the zonally averaged meridional flux of $\hat{u}$-angular momentum $\overline{\rho}\hat{v}\hat{u}\, a \cos\phi$ and of eddy angular momentum $\overline{\rho u'v'}\, a \cos\phi$. The magnitude of Ω-angular momentum flux, which is not shown, is about two orders of magnitude larger than that of the $\hat{u}$-angular momentum, particularly in lower latitudes. However, the flux of Ω-angular momentum in the upper layer is opposite from that in the lower layer. Consequently, the net meridional flux of Ω-angular momentum across each latitude circle is small when the Ω-angular momentum fluxes at both levels are summed. On the other hand, the $\hat{u}$-angular momentum is transported approximately in the same direction at each level as seen from figure 12, though the magnitude of the $\hat{u}$-angular momentum flux in the upper layer is larger than that in the lower layer. Also, the eddy fluxes of angular momentum are directed approximately in the same direction at both levels. Comparing the two flux distributions on figure 12, we see that the meridional transport of angular momentum in higher latitudes is primarily due to large-scale eddies (Starr and White 1951) and that in lower latitudes is primarily due to a direct Hadley-type circulation (Palmén and Alaka 1952).
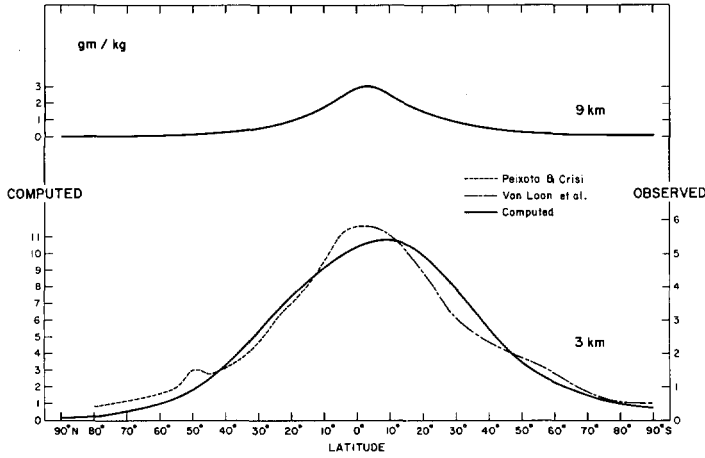
FIGURE 10.—Computed and observed January zonal mean specific humidity, q. The computed scale is on the left, and the observed scale is on the right in gm kg^{-1}.

FIGURE 11.—Time variation of the global average absolute angular momentum $\overline{\rho m}$ at 3 and 9 km from day 21 to day 80.

To facilitate comparison with observed data, we plotted on figure 13 the meridional flux of relative angular momentum $\overline{u'v'}$. The observed data for the Northern Hemisphere were obtained from Starr and White (1951), Buch (1954), and Holopainen (1967); while for the Southern Hemisphere, it was obtained from Obasi (1963) and Kidson et al. (1969). We see that the computed result underestimates the magnitude of flux in midlatitudes and probably somewhat overestimates it in the Tropics.

Figure 14A shows the latitudinal distributions of the vertical flux of eddy momentum, $\overline{\rho w'u'}\cos\phi$ and of Ω-angular momentum $\overline{\rho \hat{w}\Omega}\, a^2 \cos^2\phi$. Figure 14B shows $\overline{\rho\hat{w}\hat{u}}\, a \cos\phi$ at the middle level. Here again we see the presence of Hadley-type direct circulation in the Tropics. Note that the magnitude of vertical flux of eddy momentum is very much larger than that of $\hat{u}$-momentum even in the Tropics.

Finally, we will discuss the last term of equation (65) in vertically integrated form since in this form it represents the torque on the atmosphere by the frictional drag at the ground. After multiplying (65) by $a \cos\phi$ and integrating the resulting equation first vertically and then Pole to Pole and using equation (67), we obtain

$$\int_{-\pi/2}^{\pi/2}\int_{0}^{z_T}\frac{\partial}{\partial t}(\overline{\rho\hat{m}})a\cos\phi\,dzd\phi=-\int_{-\pi/2}^{\pi/2}\overline{\tau_\lambda}a^2\cos^2\phi\,d\phi. \quad (68)$$

Note that our form of $(\overline{F_\lambda})_H$, defined earlier, vanishes when it is integrated over the entire globe. Since the term on the left-hand side of (68) approximately vanishes during the latter 60 days, the left-hand side must also vanish. Figure 15 shows the 60-day mean of $\overline{\tau_\lambda}$ as a function of latitude. Having easterlies ($\overline{\tau_\lambda}<0$) in the Tropics and westerlies ($\overline{\tau_\lambda}>0$) in the midlatitudes, the left-hand side of (68) approximately vanishes. In the same figure, we show observed data that are taken from Obasi (1963) (annual), Priestley (1951) (winter), Gilman (1963) (annual), Hellerman (1967) (annual), and Hidaka (1958) (annual).
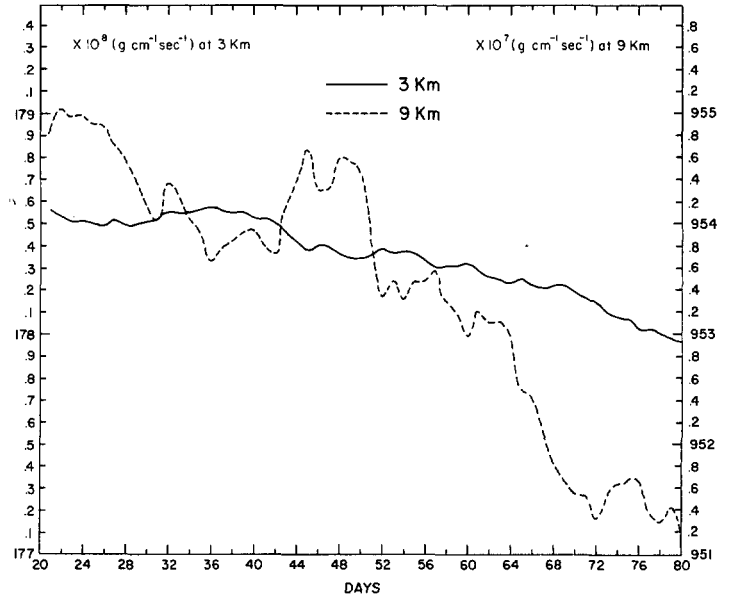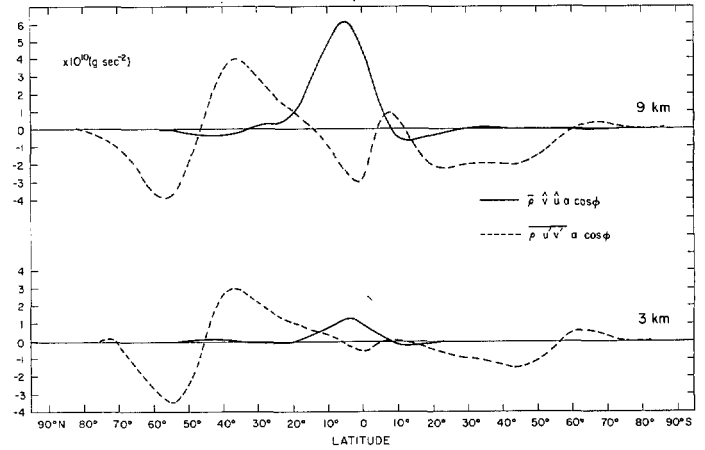

FIGURE 12.—Latitudinal distributions of the zonally averaged meridional flux of $\hat{u}$-angular momentum and eddy angular momentum.

We see that the computed stress underestimates the observed by about a factor of 2. In this computation, we assumed the drag coefficient C_D to be 3×10^{-3}.

9. MOISTURE BALANCE

Applying the zonal mean operator (63) to the water vapor flux equation (29), we obtain, in a manner similar to (65), the zonally averaged equation of the moisture per unit volume

$$\frac{\partial}{\partial t}(\overline{\rho\hat{q}})=-\frac{1}{a\cos\phi}\frac{\partial}{\partial\phi}\,[(\overline{\rho\hat{q}\hat{v}}+\overline{\rho q'v'})\cos\phi]$$

$$-\frac{\partial}{\partial z}[\overline{\rho\hat{q}\hat{w}}+\overline{\rho q'w'}]+\overline{M}+\overline{\rho E} \quad (69)$$

where the first two terms within the brackets represent the contribution of fluxes due to the mean motion and the
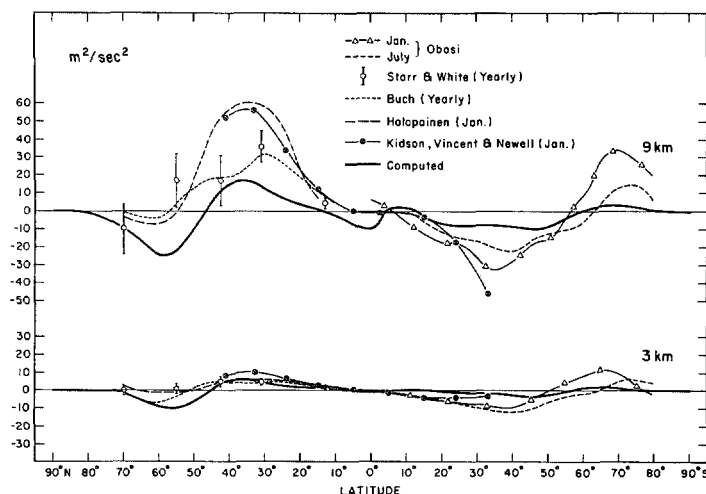
FIGURE 13.—Comparison between computed and observed latitudinal distributions of the zonally averaged meridional flux of the northward transport of relative angular momentum $\overline{u'v'}$. The solid line denotes the computed result. Note that the Southern Hemisphere summer and winter half-year data of Obasi are indicated by January and July, Obasi.

second two terms within the brackets represent the fluxes due to eddy motions.

Figure 16 shows the latitudinal distributions of the zonally averaged meridional flux of water vapor due to the mean circulation $\overline{\rho}\hat{q}\hat{v}$ cos ϕ and due to eddy motions $\overline{\rho q'v'}$ cos ϕ, respectively. Figure 17 shows the zonally averaged vertical flux of water vapor due to the mean circulation $\overline{\rho}\hat{q}\hat{w}$ and due to eddy motions $\overline{\rho q'w'}$, respectively. Figures 16 and 17 clearly indicate the important role of the mean circulation in the Tropics and the important role of eddy motions in transporting water vapor in middle latitudes.

Figure 18 shows a comparison between the computed result and the observed data of $\overline{qv}$ at the lower level. The sources of observed data are Peixoto and Crisi (1965) for the Northern Hemisphere and Starr et al. (1969) for both hemispheres. As pointed out by Starr et al. (1958), the zonally averaged meridional water vapor flux shows large seasonal changes in the Tropics. This may be why there is a large discrepancy between the yearly data of Starr et al. (1969) and the Northern Hemisphere winter data of Peixoto and Crisi (1965) in the Tropics. Our computed result generally agrees with the observed data, although the role of the mean Hadley-type circulation is over-emphasized by the fact that our computed specific humidity is about twice as large as observed, as pointed out in section 7.

For a steady state, the term on the left-hand side of equation (69) vanishes. If we integrate (69) vertically from $z=0$ to $z=z_T$, the vertical flux term vanishes because of boundary conditions on w. Thus, we can estimate the amount
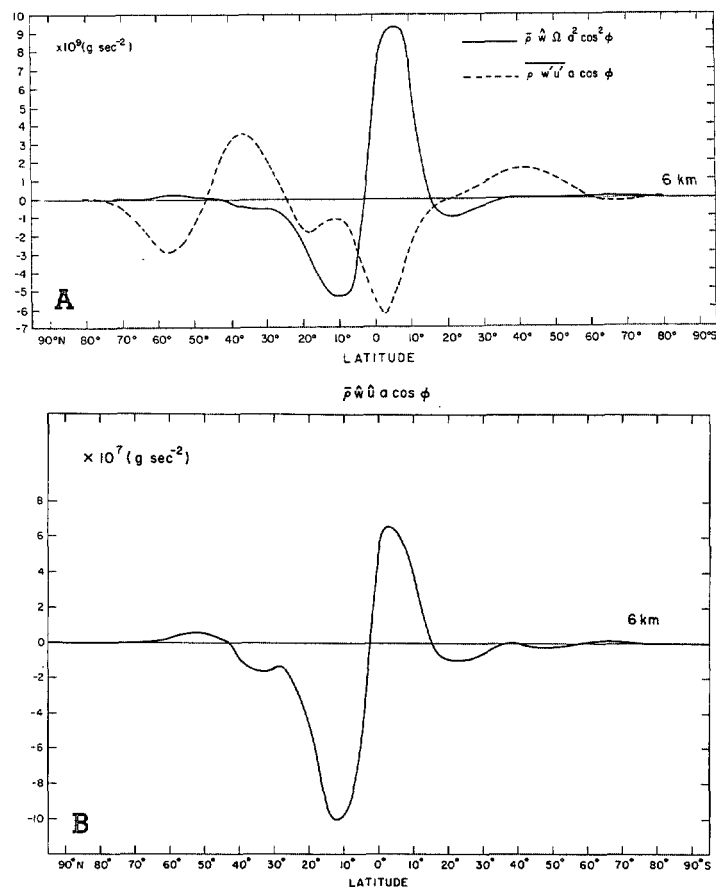
$$\int_0^{z_T} (\overline{M}+\overline{\rho E})dz$$

FIGURE 14.—Latitudinal distributions of the vertical flux of (A) Ω-angular momentum and eddy momentum and (B) $\hat{u}$-angular momentum.
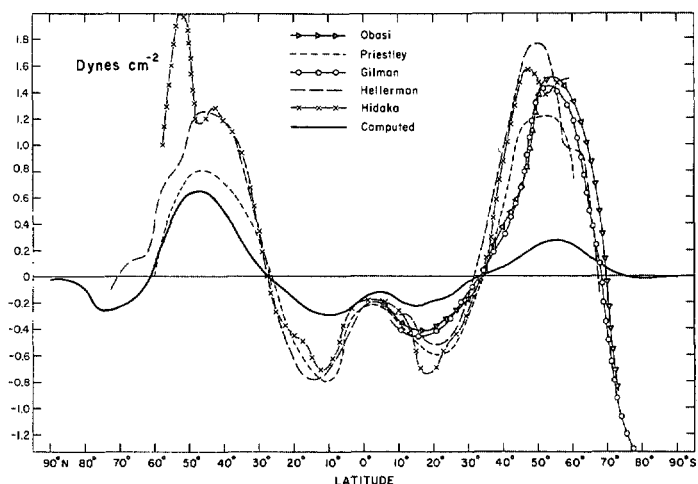

FIGURE 15.—Comparison between computed and observed latitudinal distributions of the mean zonal stress $\overline{\tau}_\lambda$. The solid line shows the computed result.

in units of gm cm^{-2} sec^{-1} using equation (69) for steady-state conditions. This quantity is the difference between evaporation and precipitation for a unit area. Figure 19 shows the latitudinal distribution of the computed difference
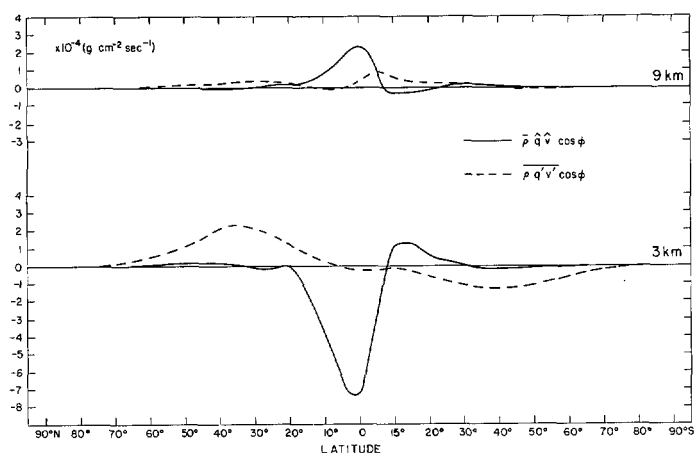
FIGURE 16.—Latitudinal distributions of the zonally averaged meridional flux of water vapor by the mean circulation and by the eddy motions.
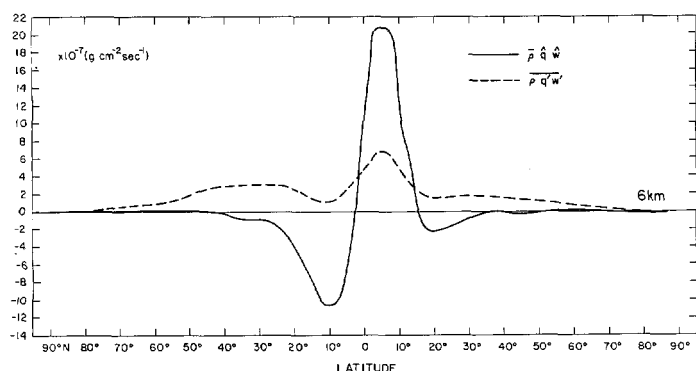

FIGURE 17.—Latitudinal distributions of the zonally averaged vertical flux of water vapor by the mean circulation and by the eddy motions.
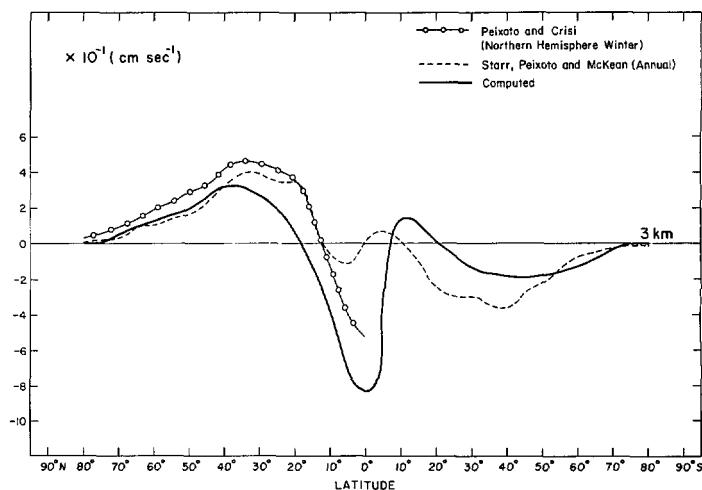

FIGURE 18.—Comparison between computed and observed latitudinal distributions of the zonally averaged values of the mean meridional transport of water vapor, $\overline{qv}$. The solid line shows the computed result.
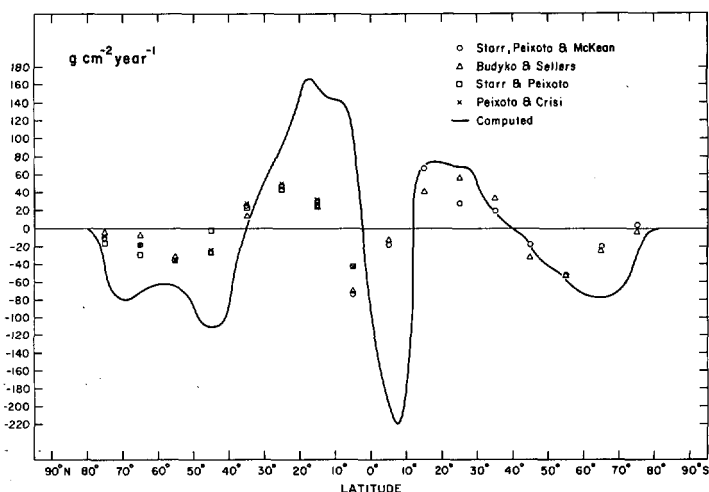

FIGURE 19.—Comparison between computed and observed latitudinal distributions of the zonally averaged evaporation minus precipitation. The solid curve shows the computed result.

between evaporation and precipitation in units of gm cm^{-2} yr^{-1}. Note that precipitation exceeds evaporation over a narrow zone in the Tropics and over latitudes north of 35° and south of 40°. On the same figure, observed data are plotted that are estimated from Budyko (1958), Starr and Peixoto (1958) and Peixoto and Crisi (1965) as given by Starr et al. (1959) and Sellers (1965). These results were obtained from yearly data. Therefore, observed data show near symmetry with respect to the Equator. Although the calculated value is about twice as large as observed data (since the calculated specific humidity is twice as large as observed), the calculated distribution is generally in good agreement with the observed data.

10. ZONAL DISTRIBUTIONS OF HEATING/COOLING RATES

The rate of heating/cooling Q in the model consists of the following five parts:

$$Q=(Q_d)_v+(Q_d)_H+Q_{al}+Q_{as}+Q_c \qquad (70)$$

where

$(Q_d)_v$ = vertical diffusion of sensible heat,
$(Q_d)_H$ = horizontal diffusion of sensible heat,
Q_{al} = long-wave radiational cooling of the atmosphere,
Q_{as} = atmospheric heating due to absorption of solar radiation by water vapor, and
Q_c = latent heating due to large-scale vertical motions.

The first term on the right-hand side of equation (70) is the divergence of vertical heat flux given in (2.22) of paper I. This type of formulation not only includes sensible heat flux but also convective latent heat flux through counter-gradient heat flow, as discussed in section 2. We see in figure 20 the latitudinal distribution of $(Q_d)_v$ at 3 km with values ranging from 0.8°C/day in the Tropics to negligible values in the polar regions. Note
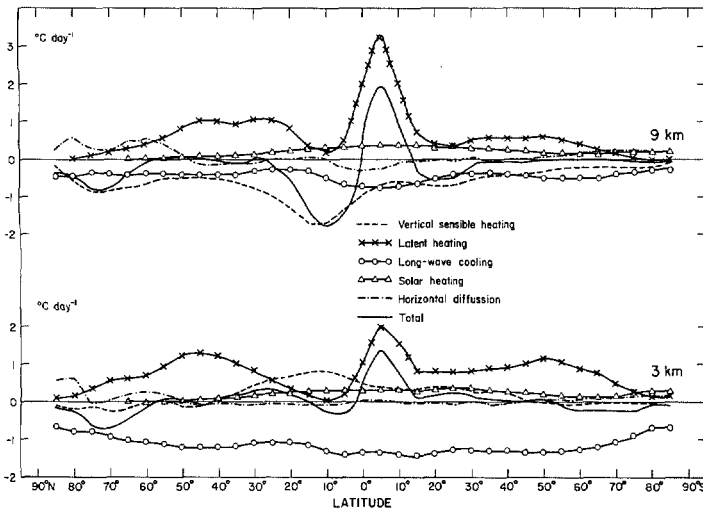
FIGURE 20.—Latitudinal distributions of heating/cooling rates at 3 and 9 km in deg day^{-1}.

that the convective adjustment, which we discussed in section 2, plays the major role of redistributing heat upward within the model without adding net heating; whereas the vertical diffusion of heat can have either a net heating or cooling effect within a vertical column.

The distribution of latent heating due to large-scale vertical motion given by equation (37) is also shown in figure 20. Here, we see a maximum near the Tropics with secondary maxima in midlatitudes. The secondary maxima are due to latent heat released in baroclinic disturbances. We note an excess amount of latent heating at 9 km in the Tropics. Since we have limited the latent heating to upward motion areas, we see the obvious manifestation of the three-cell mean circulation which would yield two upward zones, one in the tropics and the other in midlatitudes.

Long-wave cooling is also shown in figure 20. As expected, this cooling is large at 3 km with a maximum near the Tropics. At 9 km, long-wave cooling is about half of that at 3 km.

The contribution to atmospheric heating due to absorption of insolation by water vapor is shown in figure 20. We first note that the sunlight does not reach above 68°45' for mid-January. Since it is summer in the Southern Hemisphere, we expect a maximum south of the Equator of about 0.4°/day. The position of this maximum has a great deal to do with determining the location of the ascending branch of the Hadley circulation. We will expand on this point in subsequent papers when we discuss the simulation of other seasons.

The horizontal diffusion of heat given in (2.22) of paper I has very small zonal mean values. It is smaller in magnitude than the other terms.

Finally, in figure 20 we show the total heating/cooling rate that is the sum of the five parts.

11. ENERGETICS

Since this particular experiment was started from an isothermal atmosphere, at the onset there was a net warming in low latitudes and a net cooling in higher latitudes in the atmosphere. This differential heating is the basic driving mechanism of atmospheric motion. One useful way to reveal the mechanism of the atmospheric motion is to investigate the energetics of the system.

We discussed in paper I a partition of the total energy into three parts: the sum of zonal kinetic energy and zonal potential energy $\overline{K}+\overline{P}$, eddy kinetic energy K', and zonal internal energy $\overline{I}$, which are defined as:

$$\overline{K}=\tfrac{1}{2}\overline{\rho}(\hat{u}^2+\hat{v}^2) \qquad \text{(zonal kinetic energy)}, \qquad (71)$$

$$\overline{P}=g\overline{\rho}z \qquad \text{(zonal potential energy)}, \qquad (72)$$

$$K'=\tfrac{1}{2}\overline{\rho(u'^2+v'^2)} \qquad \text{(eddy kinetic energy), and} \qquad (73)$$

$$\overline{I}=c_v\overline{\rho}\hat{\overline{T}} \qquad \text{(zonal internal energy)} \qquad (74)$$

where $(\overline{\ })$ and $(\hat{\ })$ are the zonal average and the density weighted means defined in paper I. We have not attempted to separate $\overline{K}$ and $\overline{P}$ because there is a certain arbitrariness in defining energy transformation functions between $\overline{I}\leftrightarrow \overline{K}$ and $\overline{I}\leftrightarrow\overline{P}$. Also, as explained in section 5 of paper I, we have not defined an eddy internal energy that would be somewhat equivalent to available potential energy as introduced by Lorenz (1955).

The conversion functions $C(\alpha,\beta)$ of energy between the different forms of energy α and β are, as derived in paper I,

$$C(\overline{K}+\overline{P}, K')=-\overline{\rho u'v'}\,\frac{\cos\phi}{a}\,\frac{\partial}{\partial\phi}\left(\frac{\hat{u}}{\cos\phi}\right)-\overline{\rho v'^2}\,\frac{1}{a}\frac{\partial\hat{v}}{\partial\phi}$$
$$+\frac{\tan\phi}{a}\,\hat{v}\,\overline{\rho u'^2}-\overline{\rho u'w'}\,\frac{\partial\hat{u}}{\partial z}-\overline{\rho v'w'}\,\frac{\partial\hat{v}}{\partial z}, \qquad (75)$$

$$C(\overline{I}, \overline{K}+\overline{P})\doteq-\overline{\rho}\hat{w}\hat{T}\left(\frac{R}{\overline{\rho}}\frac{\partial\overline{\rho}}{\partial z}\right), \qquad (76)$$

$$C(\overline{I}, K')\doteq-\overline{\rho w'T'}\left(\frac{R}{\overline{\rho}}\frac{\partial\overline{\rho}}{\partial z}\right). \qquad (77)$$

In deriving (76) and (77), approximations are introduced as discussed in section 5 of paper I. The value of $C(\alpha,\beta)$ is positive if there is an energy transfer from α to β.

The basic energy equations used, as derived in section 5 of paper I, are summarized as:

$$\frac{\partial}{\partial t}(\overline{K}+\overline{P})+\nabla_3\cdot(\overline{K}+\overline{P}+\overline{p})\hat{\mathbf{V}}_3+\frac{1}{a\cos\phi}\frac{\partial}{\partial\phi}\,[(\hat{u}\overline{\rho u'v'}$$
$$+\hat{v}\overline{\rho v'^2})\cos\phi]+\frac{\partial}{\partial z}\,[\hat{u}\overline{\rho u'w'}+\hat{v}\overline{\rho v'w'}]$$
$$=-C(\overline{K}+\overline{P}, K')+C(\overline{I}, \overline{K}+\overline{P})+\hat{\mathbf{V}}\cdot\mathbf{F}, \qquad (78)$$
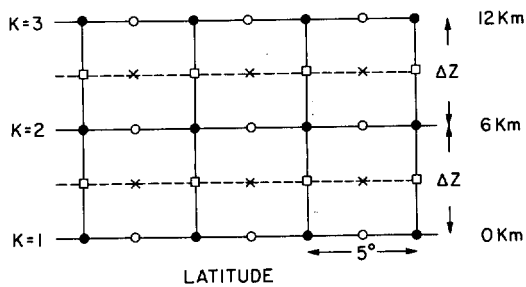
FIGURE 21.—Diagram showing where various components of the energy equations are computed. The squares show where the horizontal fluxes are computed; the circles where the vertical fluxes are computed; and the crosses where the sources, sinks, time changes, and conversions of energy are computed.

$$\frac{\partial K'}{\partial t}+\overline{\nabla}_3 \cdot (K'\overset{\wedge}{\mathbf{V}}_3)+\overline{\nabla}_3 \cdot (\overline{p\mathbf{V}'_3})+\frac{1}{a \cos \phi}\frac{\partial}{\partial \phi}\,[\tfrac{1}{2}(\overline{\rho u'^2 v'}$$

$$+\overline{\rho v'^3})\cos \phi]+\frac{\partial}{\partial z}\,[\tfrac{1}{2}(\overline{\rho u'^2 w'}+\overline{\rho v'^2 w'})]$$

$$= C(\bar{I}, K')+C(\overline{K}+\overline{P}, K')+\overline{\mathbf{V}\cdot\mathbf{F}}-\overset{\wedge}{\mathbf{V}}\cdot\mathbf{F}, \quad (79)$$

and

$$\frac{\partial \bar{I}}{\partial t}+\overline{\nabla}_3 \cdot (\bar{I}\,\overset{\wedge}{\mathbf{V}}_3)+\frac{1}{a \cos \phi}\frac{\partial}{\partial \phi}\,[(c_v\overline{\rho T' v'})\cos \phi]+\frac{\partial}{\partial z}\,(c_v\overline{\rho T' w'})$$

$$=-C(\bar{I}, K')-C(\bar{I}, \overline{K}+\overline{P})+\overline{\rho Q}. \quad (80)$$

The local time change, energy conversions, and sources and sinks of energy are computed at the center of the box, denoted by crosses in figure 21. Solid dots and squares are the grid points at the integer and half-integer levels. The box has the dimension of $\Delta z \times 5°$ latitude. The flux divergence terms in the energy equations are all computed from the vertical and horizontal fluxes at the top and bottom of the box and at the sides of the box, respectively.

Figures 22A–22D show the time variation of various global mean energy quantities for the period of 21 days to 80 days. First, the time variation of $\overline{K}$ is small in the upper layer; but in the lower layer, $\overline{K}$ increases approximately 20 percent during this period. The variations of $\overline{P}$ and $\bar{I}$ show a general decrease of less than 0.5 percent during the period. However, the day-to-day variation of K' is much larger than the overall change from the beginning to the end of this period. From a visual inspection, one notices that the period of time varation is approximately 10 days in the upper layer and somewhat shorter in the lower layer. The time variation of K' is presumably related to baroclinic activity.

Let us examine the various terms on the right-hand side of equation (78). The terms $C(\overline{K}+\overline{P}, K')$, $C(\bar{I}, \overline{K}+\overline{P})$,

and $\overset{\wedge}{\mathbf{V}} \cdot \overline{\mathbf{F}}$ are shown in figures 23, 24, and 25, respectively. Figure 23 shows that the mean flow is feeding the eddies in the Tropics and vice versa in midlatitudes. Small magnitudes of $C(\overline{K}+\overline{P}, K')$ around 45° N. may be responsible for producing a weak midlatitude westerly in the Northern Hemisphere as shown in figure 7. The magnitude of $C(\overline{K}+\overline{P}, K')$ in the Southern Hemisphere is generally too small, indicating a noticeable failure in producing strong westerlies in the Southern Hemisphere. Figure 24 shows that $C(\bar{I}, \overline{K}+\overline{P})$ is positive in the upward branch of the Hadley circulation and negative in the downward branch. In midlatitudes, this conversion is quite small due to the relatively weaker strength of the meridional circulation. This agrees with a recent observational analysis of Kidson et al. (1969) who show that for the 24° N. to 24° S. region the largest energy conversion rate is associated with kinetic energy production by mean meridional circulation. The frictional dissipation term $\overset{\wedge}{\mathbf{V}} \cdot \overline{\mathbf{F}}$ shows two minima, one in the downward branch of the Hadley circulation and the other in the midlatitude westerlies.

Figures 26A–26C show the various flux divergence terms contributing to the time change of $\overline{K}+\overline{P}$ shown on the left-hand side of equation (78).

In figure 26C, the latitudinal distribution of the vertical flux divergences is shown only at a 9-km level. For the distribution at 3 km, the sign of the value must be reversed. One notices in figures 26A–C an approximate balance in the term $\overline{\nabla}_3 \cdot (\overline{K}+\overline{P}+\overline{p})\overset{\wedge}{\mathbf{V}}_3$. For example, the term $(a \cos \phi)^{-1}\,\partial[\overline{p}\hat{v}\cos \phi]/\partial \phi$ is nearly compensated by $\partial(\hat{w}\overline{p})/\partial z$. The same general pattern holds to some extent for the other three-dimensional divergence terms $\overline{\nabla}_3 \cdot (\overline{K}\overset{\wedge}{\mathbf{V}}_3)$ and $\overline{\nabla}_3 \cdot (\overline{P}\overset{\wedge}{\mathbf{V}}_3)$. Of course, what contributes to $\partial(\overline{K}+\overline{P})/\partial t$ is the sum of the flux divergence terms and the energy conversion terms, and all terms are obviously important. However, by grouping the terms on the graphs according to the same order of magnitude, one can see their relative importance as functions of latitude.

The terms on the right-hand side of the K' equation (79) are shown in figure 28 for $C(\bar{I}, K')$; in figure 23 for $C(\overline{K}+\overline{P}, K')$; and in figure 25 for $\overline{\mathbf{V}\cdot\mathbf{F}}$ and $\overset{\wedge}{\mathbf{V}}\cdot\overline{\mathbf{F}}$. Note that $\overline{\mathbf{V}\cdot\mathbf{F}}<\overset{\wedge}{\mathbf{V}}\cdot\overline{\mathbf{F}}<0$. Therefore, the term $\overline{\mathbf{V}\cdot\mathbf{F}}-\overset{\wedge}{\mathbf{V}}\cdot\overline{\mathbf{F}}$ is·negative everywhere, indicating the dissipation of energy for the K' equation. As it is now well known, the term $C(\bar{I}, K')$ is a major contributor to $\partial K'/\partial t$. Since $C(\bar{I}, K')$ represents the correlation between w' and T', we expect a maximum in midlatitudes due to baroclinic eddies, and we note a secondary maximum in the Tropics that arises from the same correlation within latent heat cells. This latter feature was also noted by Manabe and Smagorinsky (1967).

The terms on the left-hand side of the K' equation (79) are shown on figures 27A–27C. In figure 27B, the latitudinal distributions of vertical flux divergence are
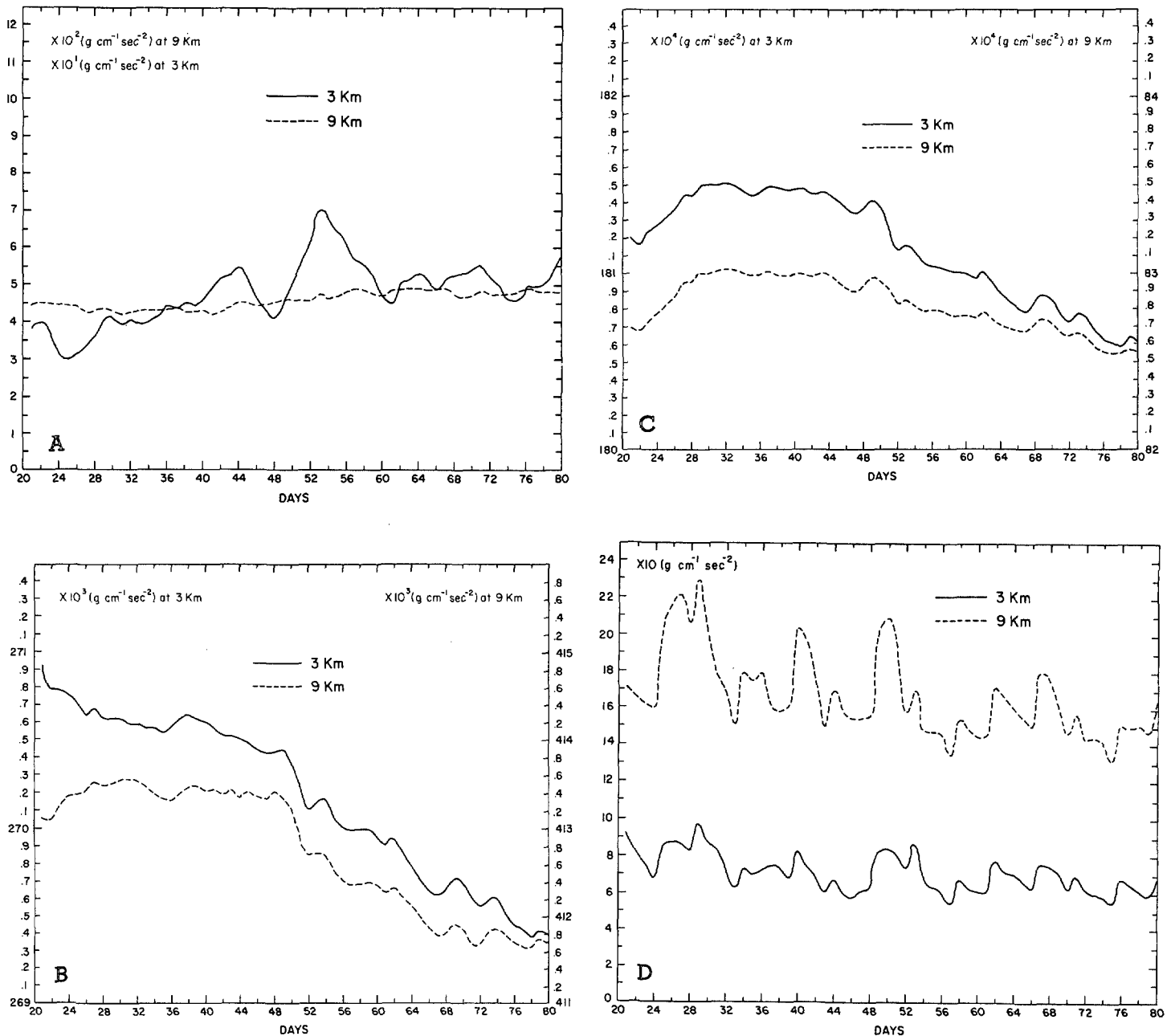
FIGURE 22.—(A) time variation of $\overline{K}$ from day 21 to day 80 at 3 and 9 km; (B) of $\overline{P}$ from day 21 to day 80 at 3 and 9 km; (C) of $\overline{I}$ from day 21 to day 80 at 3 and 9 km; and (D) of K' from day 21 to day 80 at 3 and 9 km.

shown only at a 9-km level. For the distribution at 3 km, the sign of the values must be reversed. Note that the contributions of the terms $\overline{\nabla_3 \cdot (K' \hat{V}_3)}$, $(a \cos \phi)^{-1} \partial[\frac{1}{2} \overline{(\rho u'^2 v'}$ $+ \rho v'^3)} \cos \phi]/\partial\phi$ and $\partial[\frac{1}{2} \overline{(\rho u'^2 w' + \rho v'^2 w')}]/\partial z$ are relatively small compared with $(a \cos \phi)^{-1} \partial[\overline{pv'} \cos \phi]/\partial\phi$ and $\partial(\overline{pw'})/\partial z$. The maximum of the meridional divergence of $\overline{pv'}$ in the upper layer (fig. 27A) in the Tropics may be an indication of the presence of lateral coupling associated with an equatorward flux of wave energy as recently discussed by Mak (1969). The maximum of $\partial(\overline{pw'})/\partial z$ in midlatitudes is presumably related to baroclinic activities.

The terms on the right-hand side of the $\overline{I}$ equation (80) are shown in figure 28 for $C(\overline{I}, K')$, in figure 24 for $C(\overline{I}, \overline{K}+\overline{P})$, and figure 29 for $\overline{\rho Q}$. Notice that $\overline{\rho Q}$ and $C(\overline{I}, \overline{K}+\overline{P})$ compensate each other, particularly in low latitudes.

The terms on the left-hand side of the $\overline{I}$ equation (80) are shown in figures 30A–30C. In figure 30B, only the distribution at 9 km is shown. For the distribution at 3 km, reverse the sign. Although the components of $\overline{\nabla_3 \cdot (I \hat{V}_3)}$ are large in magnitude as seen from figure 30C, the horizontal divergence and vertical divergence terms tend to be compensated. Since the vertical divergence
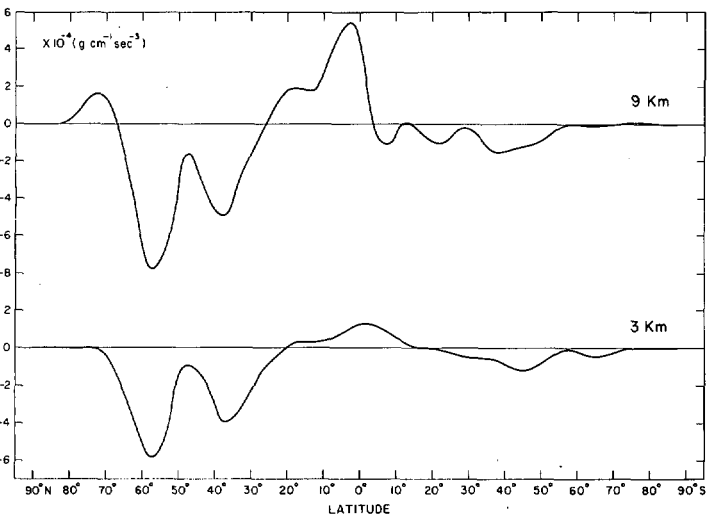
FIGURE 23.—Latitudinal distributions of the conversion term $C(\overline{K}+\overline{P}, K')$ at 3 and 9 km.
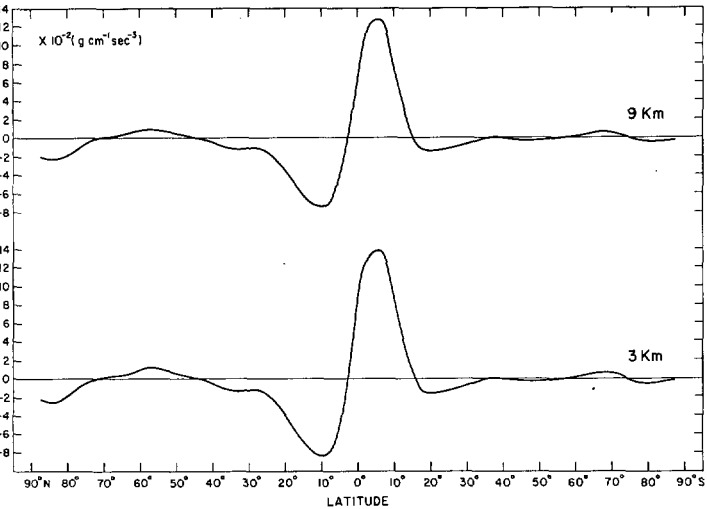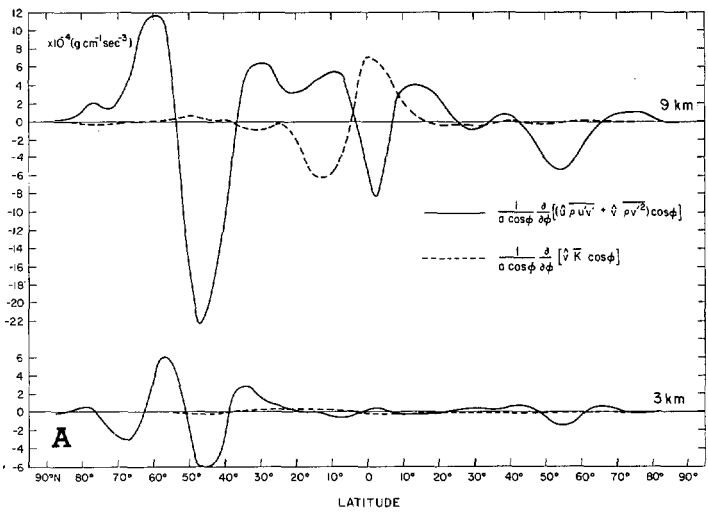

FIGURE 24.—Latitudinal distributions of the conversion term $C(\bar{I}, \overline{K}+\overline{P})$ at 3 and 9 km.
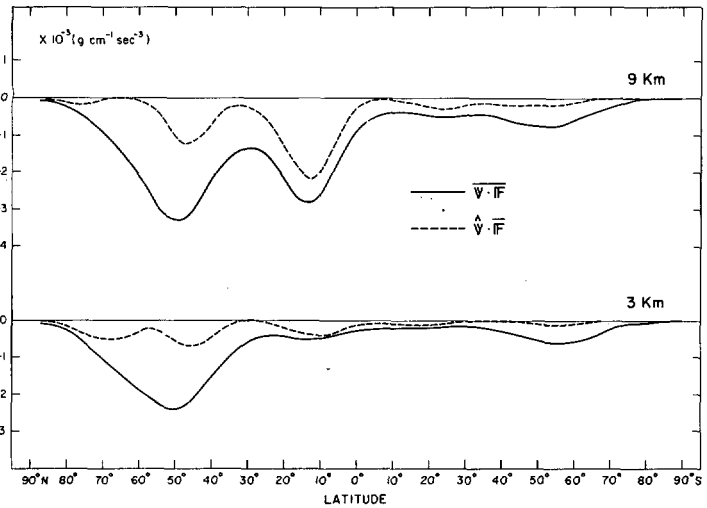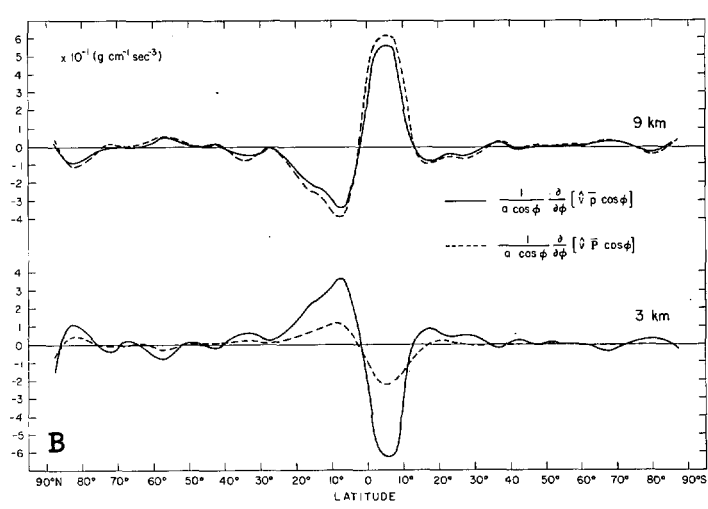

FIGURE 25.—Latitudinal distributions of frictional dissipation terms $\overline{\mathbf{V}\cdot\mathbb{F}}$ and $\hat{\mathbf{V}}\cdot\overline{\mathbb{F}}$ at 3 and 9 km.
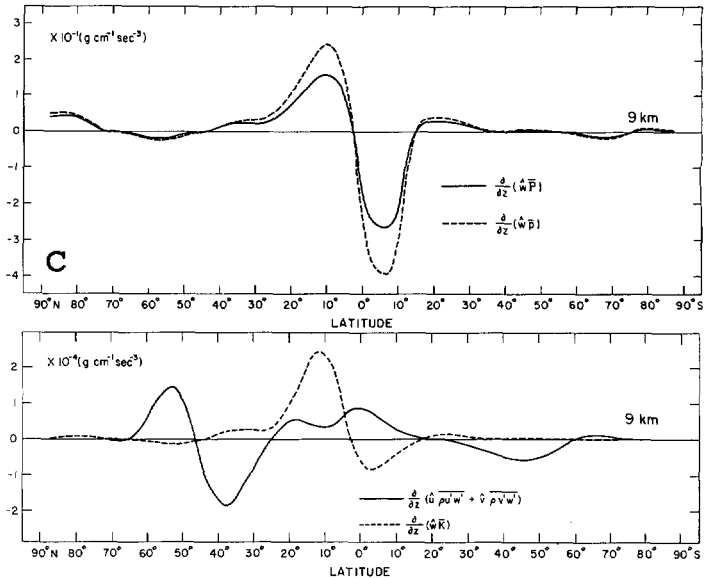
FIGURE 26.—Latitudinal distributions of various flux divergence terms in equation (78) for time change of $\overline{K}+\overline{P}$.
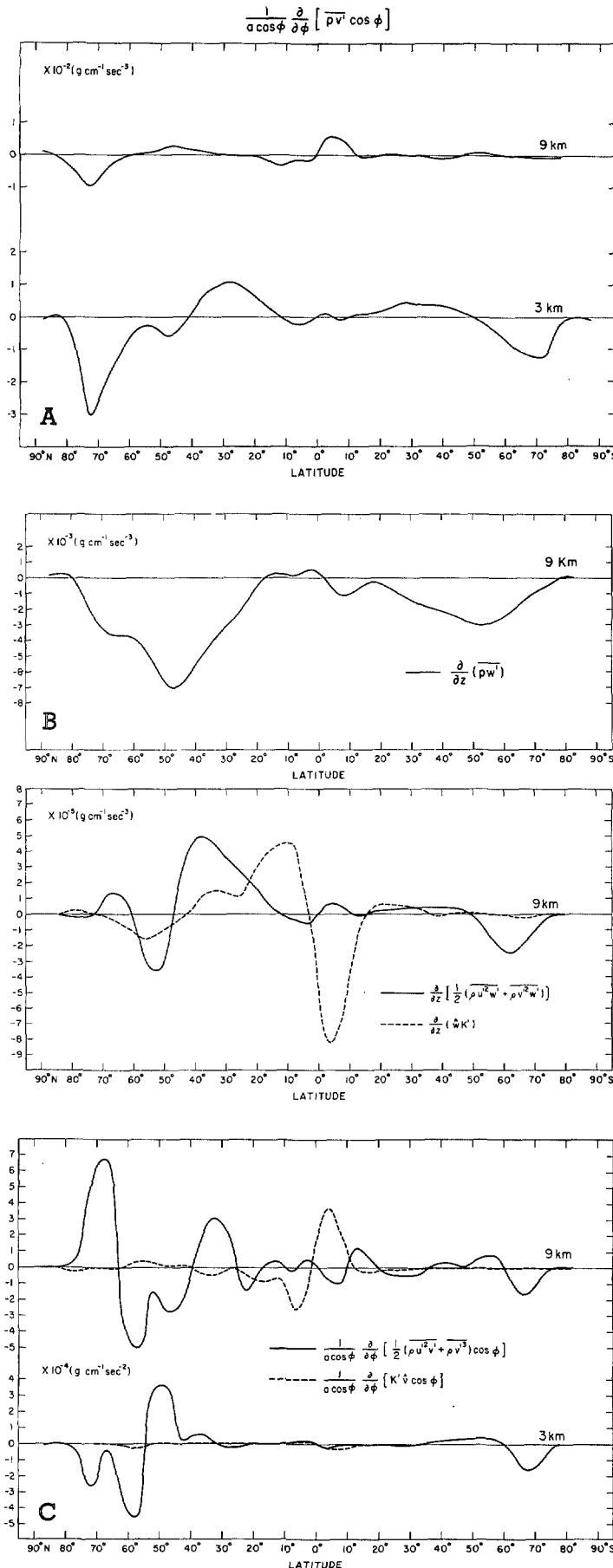
$$\frac{1}{a\cos\phi}\frac{\partial}{\partial\phi}\left[\overline{\rho v'}\cos\phi\right]$$

X10⁻²(g cm⁻¹ sec⁻³)

9 km

3 km

A

LATITUDE

X10⁻³(g cm⁻¹ sec⁻³)

9 Km

$\frac{\partial}{\partial z}(\overline{\rho w'})$

B

LATITUDE

X10⁻⁵(g cm⁻¹ sec⁻³)

9 km

$\frac{\partial}{\partial z}\left[\frac{1}{2}(\overline{\rho u'^2 w'}+\overline{\rho v'^2 w'})\right]$

$\frac{\partial}{\partial z}(\overline{\dot w K'})$

LATITUDE

X10⁻³(g cm⁻¹ sec⁻³)

9 Km

3 Km

LATITUDE

FIGURE 28.—Latitudinal distribution of the conversion term $C(\overline{I}, K')$.

X10⁻²(g cm⁻¹ sec⁻³)

9 Km

3 Km
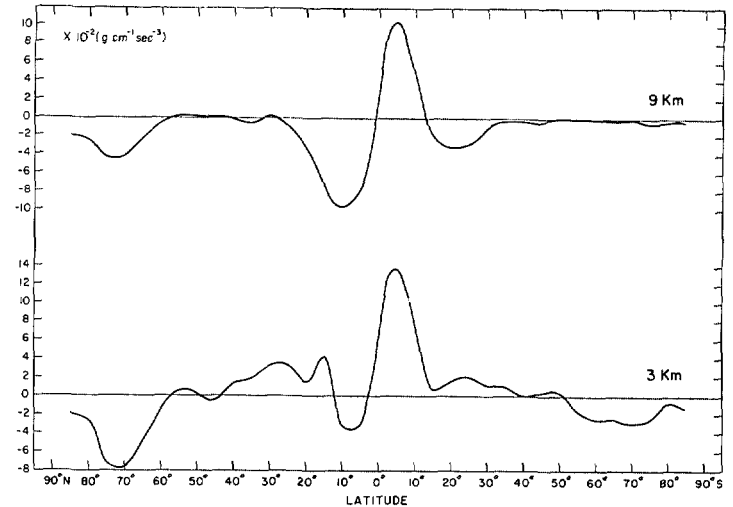
LATITUDE

FIGURE 29.—Latitudinal distribution of the total heating $\overline{\rho Q}$.

9 km

$\frac{1}{a\cos\phi}\frac{\partial}{\partial\phi}\left[\frac{1}{2}(\overline{\rho u'^2 v'}+\overline{\rho v'^3})\cos\phi\right]$

$\frac{1}{a\cos\phi}\frac{\partial}{\partial\phi}\{\overline{K'\hat v}\cos\phi\}$

X10⁻⁴(g cm⁻¹ sec⁻²)

3 km

C

LATITUDE

FIGURE 27.—Latitudinal distributions of the various flux divergence terms in equation (79) for time change of K'.

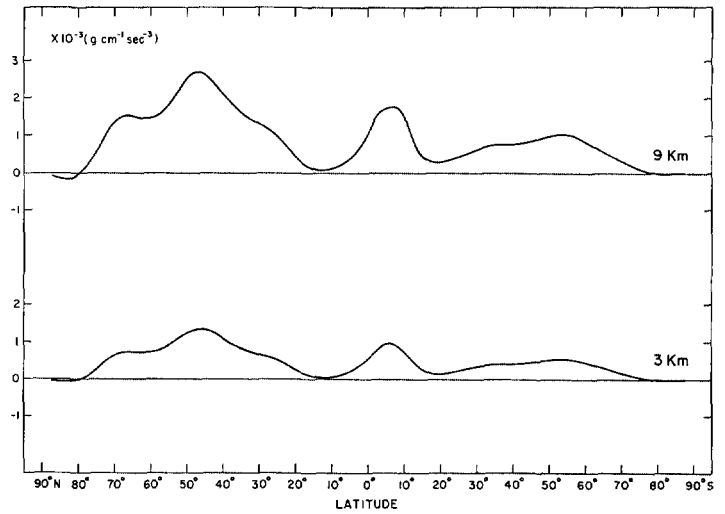of $c_v\rho\overline{T''w'}$ is still smaller than the horizontal divergence of $c_v\rho\overline{T''v'}$ in magnitude, the latter term is the important term on the left-hand side of equation (80). Our values of poleward sensible heat transport $\overline{T''v'}$ are compared with those computed from observed data as shown in figure 31. The observed data are based on: Wiin-Nielsen et al. (1964) (January 1963), Peixoto (1960) (annual), Mintz (1955) (annual), and Kidson et al. (1969). We find that poleward transport of sensible heat by the eddies in the model is smaller than observed.

Finally, we shall present the energy flow diagram for the model in figure 32. The solid line indicates the direction of energy flow based on observed data as discussed in paper I. The asterisk for the conversion terms indicates that the quantity in question is integrated vertically throughout the depth of the atmosphere. The numerals directly under the conversion terms show "observed"
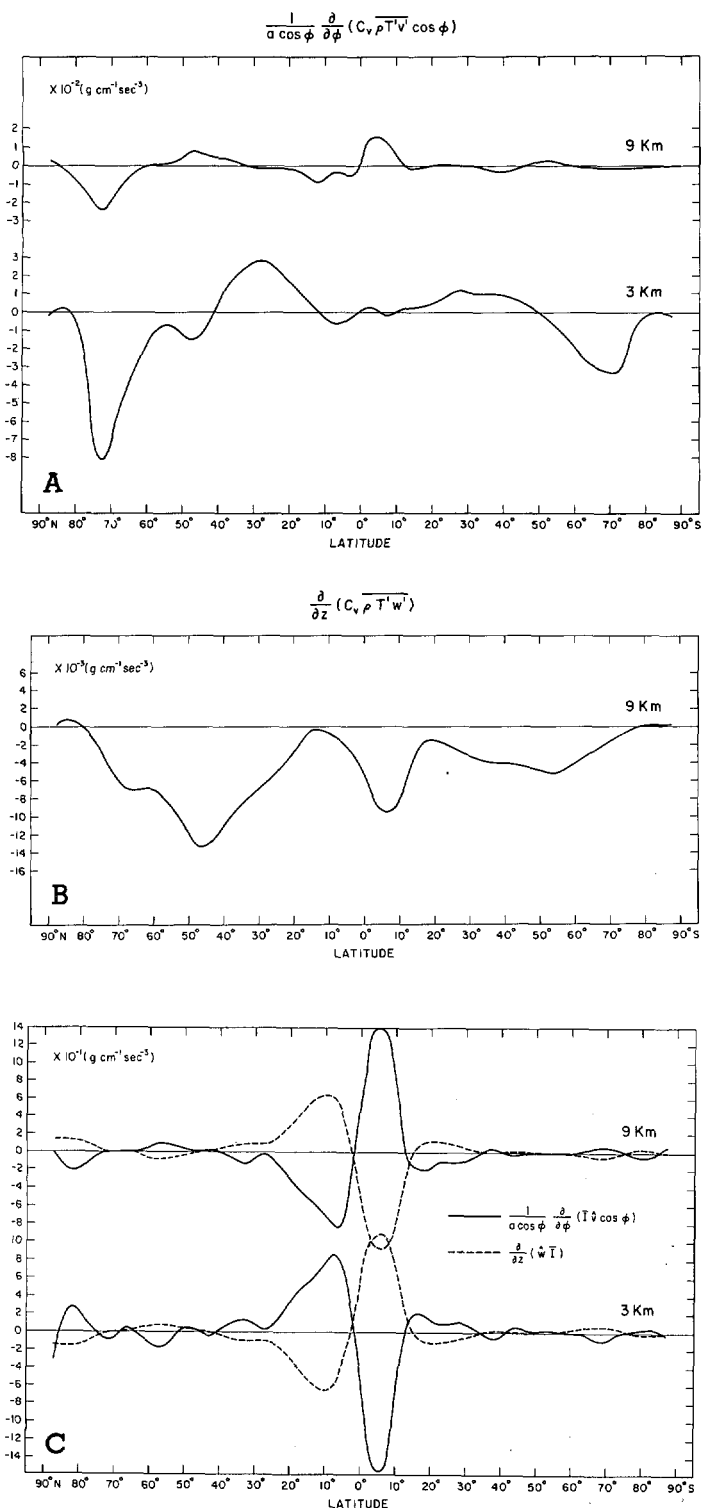
$$\frac{1}{a\cos\phi}\frac{\partial}{\partial\phi}(C_v\,\overline{\rho T'v'}\cos\phi)$$

$$\frac{\partial}{\partial z}(C_v\,\overline{\rho\,T'w'})$$

FIGURE 30.—Latitudinal distributions of the various flux divergence terms in equation (80) for time change of $\overline{I}$.
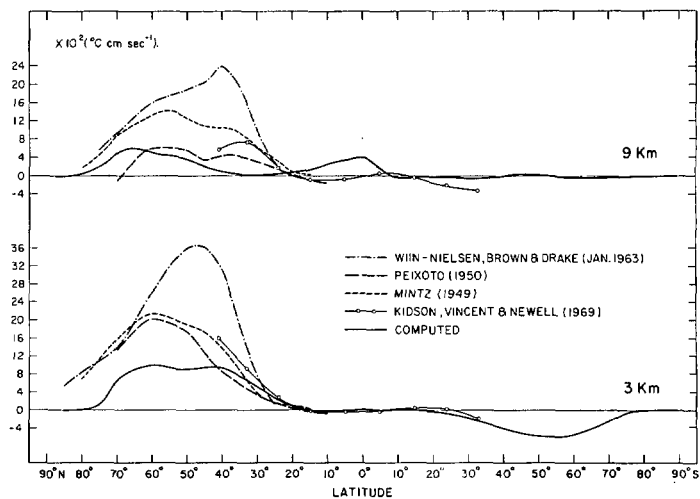

FIGURE 31.—Comparison between computed and observed latitudinal distributions of northward eddy transport of heat $\overline{T'v'}$. The solid curve shows the computed result.
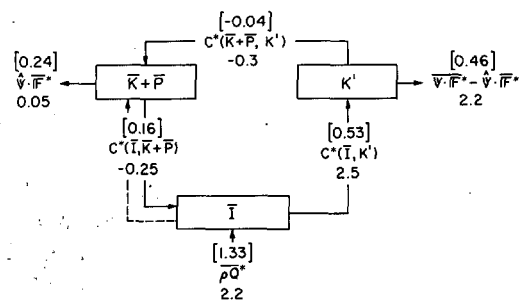

FIGURE 32.—Energy flow diagram for the model. The units are w m^{-2}. The computed values are shown in brackets and "observed" estimates are shown under the various quantities.

estimates in units of w m^{-2} ($=10^3$ ergs cm^{-2} sec^{-1}) based on data listed in paper I. The computed values are shown in brackets in the same units directly above the conversion terms. The observed estimates are forced in balance, and the values for the dissipations as obtained are residual. No adjustment has been made on the computed values. Although the balances of energy conversion terms for the $\overline{K}+\overline{P}$ box and the K' box are generally good, the bal-

ance is off by approximately 50 percent for the $\overline{I}$ box. This may be explained by truncation errors in numerical computations that result in weak baroclinic activities. With one exception, the direction of energy flow for the model agrees with that of the observations. The exception is in the conversion of energy from the $\overline{I}$ box to the $\overline{K}+\overline{P}$ box as indicated by the dashed line in figure 32. The reason for the discrepancy is that this conversion term is strongly controlled by the direct meridional circulation in the Tropics as shown recently by Kidson et al. (1969) and that this region of the globe is usually not taken into account in the observed estimates. As seen from figure 24, if the region covering 15° N. to 15° S. is excluded in the computation of $C(\overline{I},\ \overline{K}+\overline{P})$, then the direction of energy flow is from the $\overline{K}+\overline{P}$ box to the $\overline{I}$ box, as indicated by the solid arrow.

For energy values we have $\overline{I}=32\times10^{11}$, $\overline{P}=82\times10^{10}$, $\overline{K}=6\times10^8$, and $K'=3\times10^8$, all in units of ergs cm^{-2}. The value of $\overline{K}$ agrees with the observed estimate given for example by Oort (1964), but the value of K' is about half the amount of the observed value, again indicating the weak eddy activity of the model.

12. CONCLUSIONS

Let us now recapitulate the results of this simulation experiment. We prescribed a January mean sea level earth's surface temperature distribution that was held constant in time. The initial atmosphere was at rest, dry and isothermal (240°K). After an initial period of essentially a direct circulation, the flow in midlatitudes broke down into baroclinic waves that gave typical midlatitude high- and low-pressure patterns. The direct tropical cell transported heat, angular momentum, moisture, and energy vertically and horizontally in the Tropics. The baroclinic waves in the midlatitude indirect cell transported heat, angular momentum, moisture, and energy poleward. What resulted from this circulation are many of the features of the observed climatology; however, there were many shortcomings. The discrepancy with observed features should be explained when additional physical processes are added to the model and finite-difference grids are refined.

Presently, we are running several versions of the model atmosphere extending up to an 18-km height with the vertical height increment of 3 km. The results of the six-layer version show much improvement over those of the two-layer version. Even for the two-layer version, incorporation of the earth's orography and ground temperature calculations into the model has improved the computed climatology (Kasahara and Washington 1969).

Very recently, we have extended the top of the model atmosphere to a 36-km height using a six-layer version with $\Delta z = 6$ km. The lower two layers correspond, geometrically speaking, to the model atmosphere of the two-layer version presented in this paper. The tropospheric structure with this six-layer model is much improved over that of the two-layer version.

The finite-difference schemes for these various versions of the model are basically all the same as described in this paper, except for handling of the earth's orography.

We should also add that the two-layer version of the model has been tested by Baumhefner (1970) for global real data numerical forecasts. Despite the rather simple geometry of the model, the forecasting usefulness of the two-layer model is judged to be approximately 48 hr for the surface pressure and 96 hr for the 6-km or midtropospheric pressure. Recent tests by Baumhefner (1969) indicate that the use of a six-layer version has increased the forecasting skill by 10 percent over that of the two-layer version.

REFERENCES

Baumhefner, David P., "The Real Data Forecast Project at NCAR—A Progress Report," *Proceedings of the Meteorological Technical Exchange Conference, USAF Air Weather Service, Colorado Springs, Colorado, July 14-17, 1969*, Air Weather service U.S. Air Force, Oct. 1969, pp. 123-137.

Baumhefner, David P., "Global Real-Data Forecasts With the NCAR Two-Layer General Circulation Model," *Monthly Weather Review*, Vol. 98, No. 2, Feb. 1970, pp. 92-99.

Buch, Hans S., "Hemispheric Wind Conditions During the Year 1950," *Final Report*, Part 2, Contract AF19(122)-153, Department of Meteorology, Massachusetts Institute of Technology, Cambridge, May 31, 1954, 126 pp.

Budyko, M. I., *Heat Balance of the Earth's Surface (Teplovoǐ balans zemnoi poverkhnosti, 1956)*, N. A. Stepanova, Translator, U.S. Weather Bureau, Washington, D.C., 1958, 255 pp.

Burdecki, Feliks, "A Study of Temperature Distribution in the Atmosphere," *Weather Bureau Notes*, Vol. 4, No. 3, Washington, D.C., 1955, pp. 192-203.

Clapp, Philip F., "Global Cloud Cover for Seasons Using TIROS Nephanalyses," *Monthly Weather Review*, Vol. 92, No. 11, Nov. 1964, pp. 495-507.

Deardorff, James W., "The Counter-Gradient Heat Flux in the Lower Atmosphere and in the Laboratory," *Journal of the Atmospheric Sciences*, Vol. 23, No. 5, Sept. 1966, pp. 503-506.

Deardorff, James W., "Empirical Dependence of the Eddy Coefficient for Heat Upon Stability Above the Lowest 50 m," *Journal of Applied Meteorology*, Vol. 6, No. 4, Aug. 1967, pp. 631-643.

DuFort, E. C., and Frankel, S. P., "Stability Conditions in the Numerical Treatment of Parabolic Differential Equations," *Math Tables and Other Aids to Computations*, Vol. 7, No. 43, National Research Council, Washington, D.C., July 1953, pp. 135-152.

Gilman, Peter A., "Indirect Measurement of the Mean Meridional Circulation in the Southern Hemisphere," *Planetary Circulation Project, Scientific Report* No. 3, Contract AF19(628)-2408, Massachusetts Institute of Technology, Cambridge, Nov. 1963, 49 pp.

Hellerman, S., "An Updated Estimate of the Wind Stress on the World Ocean," *Monthly Weather Review*, Vol. 95, No. 9. Sept 1967, pp. 607-626.

Hidaka, Koji, "Computation of the Wind Stresses Over the Oceans," *Records of Oceanographic Works in Japan*, Vol. 5, No. 2, Science Council of Japan, Tokyo, Mar. 1958, pp. 77-123.

Holopainen, E. O., "On the Mean Meridional Circulation and the Flux of Angular Momentum Over the Northern Hemisphere," *Tellus*, Vol. 19, No. 1, 1967, pp. 1-13.

Houghton, David, Kasahara, Akira, and Washington, Warren, "Long-Term Integration of the Barotropic Equation by the Lax-Wendroff Method," *Monthly Weather Review*, Vol. 94, No. 3, Mar. 1966, pp. 141-150.

Jensen, Clayton E., "Energy Transformation and Vertical Flux Processes Over the Northern Hemisphere," *Journal of Geophysical Research*, Vol. 66, No. 4, Apr. 1961, pp. 1145-1156.

Kasahara, Akira, and Washington, Warren M., "NCAR Global General Circulation Model of the Atmosphere," *Monthly Weather Review*, Vol. 95, No. 7, July 1967, pp. 389-402.

Kasahara, Akira. and Washington, Warren M., "Thermal and Dynamical Effects of Orography on the General Circulation of the Atmosphere," *Proceedings of the WMO/IUGG Symposium on Numerical Weather Prediction, Tokyo, Japan, November 26–December 4, 1968*, Meteorological Society of Japan, Tokyo, Mar. 1969, pp. IV-47—IV-56.

Kidson, John W., Vincent, Dayton G., and Newell, Reginald E., "Observational Studies of the General Circulation of the Tropics: Long Term Mean Values," *Quarterly Journal of the Royal Meteorological Society*, Vol. 95, No. 404, Apr. 1969, pp. 258-287.

Kurihara, Yoshio, and Holloway, J. Leith, Jr., "Numerical Integration of a Nine-Level Global Primitive Equation Model Formulated by the Box Method," *Monthly Weather Review*, Vol. 95, No. 8, Aug. 1967, pp. 509-530.

Lax, Peter D., and Wendroff, Burton, "Systems of Conservation Laws," *Communications on Pure and Applied Mathematics*, Vol. 13, No. 2, Interscience Publishers, Inc., New York, May 1960, pp. 217-237.

Leith, Cecil E., "Numerical Simulation of the Earth's Atmosphere," *Methods in Computational Physics: Volume 4. Applications in Hydrodynamics*, Academic Press, New York, 1965, 385 pp. (see pp. 1-28).

Lorenz, Edward N., "Available Potential Energy and the Maintenance of the General Circulation," *Tellus*, Vol. 7, No. 2, May 1955, pp. 157-167.

Lorenz, Edward N., *The Nature and Theory of the General Circulation of the Atmosphere*, World Meteorological Organization, Geneva, 1967, 161 pp.

Lumley, John L., and Panofsky, Hans A., *The Structure of Atmospheric Turbulence*, Interscience Publishers, Inc., New York, 1964, 239 pp.

Mak, Man-Kin, "Laterally Driven Stochastic Motions in the Tropics," *Journal of the Atmospheric Sciences*, Vol. 26, No. 1, Jan. 1969, pp. 41-64.

Manabe, Syukuro, and Smagorinsky, Joseph, "Simulated Climatology of a General Circulation Model With a Hydrologic Cycle: II. Analysis of the Tropical Atmosphere," *Monthly Weather Review*, Vol. 95, No. 4, Apr. 1967, pp. 155-169.

Manabe, Syukuro, Smagorinsky, Joseph, and Strickler, Robert F., "Simulated Climatology of a General Circulation Model With a Hydrologic Cycle," *Monthly Weather Review*, Vol. 93, No. 12, Dec. 1965, pp. 769-798.

Mintz, Yale "The Observed Zonal Circulation of the Atmosphere," *Bulletin of the American Meteorological Society*, Vol. 35, No. 5, May 1954, pp. 208-214.

Mintz, Yale, "Final Computation of the Mean Geostrophic Poleward Flux of Angular Momentum and of Sensible Heat in the Winter and Summer of 1949," *Final Report*, Article 5, Contract No. AF19(122)-48, Department of Meteorology, University of of California, Los Angeles, Mar. 15, 1955, 14 pp.

Mintz, Yale, "Very Long-Term Global Integration of the Primitive Equations of Atmospheric Motions," *WMO Technical Note* No. 66, World Meteorological Organization, Geneva, 1965, pp. 141-167.

Mintz, Yale, and Lang, John, "A Model of the Mean Meridional Circulation," *Final Report*, Article 6, Contract No. AF19(122)-48, Department of Meteorology, University of California, Los Angeles, Mar. 15, 1955, 10 pp.

Miyakoda, Kikuro, "Some Characteristic Features of Winter Circulation in the Troposphere and the Lower Stratosphere," *Technical Report* No. 14, Contract No. NSF-GP-471, Department of the Geophysical Sciences, University of Chicago, 1963, 93 pp.

Obasi, G. O. P., "Poleward Flux of Atmospheric Angular Momentum in the Southern Hemisphere," *Journal of the Atmospheric Sciences*, Vol. 20, No. 6, Nov. 1963, pp. 516-528.

O'Conner, James F., "Mean Circulation Patterns Based on 12 Years of Recent Northern Hemispheric Data," *Monthly Weather Review*, Vol. 89, No. 7, July 1961, pp. 211-227.

Ogura, Yoshimitsu, and Charney, Jule G., "A Numerical Model of Thermal Convection in the Atmosphere," *Proceedings of the International Symposium on Numerical Weather Prediction, Tokyo, Japan, Nov. 1960*, Meteorological Society of Japan, Tokyo, Mar. 1962, pp. 431-451.

Oort, Abraham H., "On Estimates of the Atmospheric Energy Cycle," *Monthly Weather Review*, Vol. 92, No. 11, Nov. 1964, pp. 483-493.

Palmén, Erik H., and Alaka, M. A., "On the Budget of Angular Momentum in the Zone Between Equator and 30°N," *Tellus*, Vol. 4, No. 4, Nov. 1952, pp. 324-331.

Palmén, Erik H., and Newton, C. W., *Atmospheric Circulation Systems*, Academic Press, New York, 1969, 603 pp.

Palmén, Erik H., Riehl, Herbert, and Vuorela, L. A., "On the Meridional Circulation and Release of Kinetic Energy in the Tropics," *Journal of Meteorology*, Vol. 15, No. 3, June 1958, pp. 271-277.

Palmén, Erik H., and Vuorela, L. A., "On the Mean Meridional Circulations in the Northern Hemisphere During the Winter Season," *Quarterly Journal of the Royal Meteorological Society*, Vol. 89, No. 379, Jan. 1963, pp. 131-138.

Peixoto, José P., "Hemispheric Temperature Conditions During the Year 1950," *Planetary Circulation Project, Scientific Report* No. 4, Contract No. AF19(604)-6108, Massachusetts Institute of Technology, Cambridge, Mass., 1960, 211 pp.

Peixoto, José P., and Crisi, A. R., "Hemispheric Humidity Conditions During the IGY," *Planetary Circulation Project Scientific Report* No. 6, Contract No. AF19(628)-2408, Massachusetts Institute of Technology, Cambridge, Mass., Nov. 1965, 166 pp.

Petterssen, Sverre, Bradbury, Dorothy L., and Pedersen, Kaare, "The Norwegian Cyclone Models in Relation to Heat and Cold Sources," *Geofysiske Publikasjoner*, Vol. 24, No. 9, 1962, pp. 243-280.

Priestley, Charles H. B., "A Survey of the Stress Between the Ocean and the Atmosphere," *Australian Journal of Scientific Research, Physical Sciences* Ser. A, Vol. 4, No. 3, Sept. 1951, pp. 315-328.

Richtmyer, Robert D., "A Survey of Difference Methods for Non-Steady Fluid Dynamics," *NCAR Technical Notes* 63-2, National Center for Atmospheric Research, Boulder, Colo., 1963, 25 pp.

Sasamori, Takashi, "Simplification of Radiative Cooling Calculation for Application to Atmospheric Dynamics," paper presented at the WMO/IUGG Symposium on Radiation, Including Satellite Techniques, Bergen, Norway, Aug. 2-28, 1968a.

Sasamori, Takashi, "The Radiative Cooling Calculation for Application to General Circulation Experiments," *Journal of Applied Meteorology*, Vol. 7, No. 5, Oct. 1968b, pp. 721-729.

Schwerdtfeger, Werner, and Martin, David W., "The Zonal Flow of the Free Atmosphere Between 10N and 80S, in the South American Sector," *Journal of Applied Meteorology*, Vol. 3, No. 6, Dec. 1964, pp. 726-733.

Sellers, William D., *Physical Climatology*, The University of Chicago Press, 1965, 272 pp.

Smagorinsky, Joseph, "General Circulation Experiments With the Primitive Equations: I. The Basic Experiment," *Monthly Weather Review*, Vol. 91, No. 3, Mar. 1963, pp. 99-164.

Smagorinsky, Joseph, Manabe, Syukuro, and Holloway, J. Leith, Jr., "Numerical Results From a Nine-Level Circulation Model of the Atmosphere," *Monthly Weather Review*, Vol. 93, No. 12, Dec. 1965, pp. 727-768.

Starr, Victor P., Peixoto, José P., and Livadas, G. C., "On the Meridional Flux of Water Vapor in the Northern Hemisphere," *Geofisica Pura e Applicata*, Vol. 39, Milan, Jan./Apr. 1958, pp. 174-185.

Starr, Victor P., Peixoto, José P., and McKean, R. G., "Pole-to-Pole Moisture Conditions," *Pure and Applied Geophysics*, Vol. 73, No. 2, **1969**, pp. 85–116.

Starr, Victor P., and White, R. M., "A Hemispherical Study of the Atmospheric Angular-Momentum Balance," *Quarterly Journal of the Royal Meteorological Society*, Vol. 77, No. 332, Apr. **1951**, pp. 215–225.

Taljaard, J. J., van Loon, H., Crutcher, H., and Jenne, R. L., "Climate of the Upper Air: Part 1. Southern Hemisphere," *Volume 1. Temperatures, Dew Points, and Heights at Selected Pressure Levels*, NAVAIR 50–1C–55, Washington, D.C., **1969**, 6 pp. plus 134 figures.

Telegadas, Kosta, and London, Julius, "A Physical Model of the Northern Hemisphere Troposphere for Winter and Summer," *Scientific Report* No. 1, Contract No. AF19(122)–165, College of Engineering, New York University, Feb. **1954**, 55 pp.

Tucker, G. B., "Mean Meridional Circulations in the Atmosphere," *Quarterly Journal of the Royal Meteorological Society*, Vol. 85, No. 365, July **1959**, pp. 209–224.

van Loon, H., Taljaard, J. J., Jenne, R., and Crutcher, H., "Climate of the Upper Air: Part 1. Southern Hemisphere," *Volume II. Zonal and Meridional Geostrophic Wind Components*, NAVAIR 50–1C–56, Washington, D.C., **1970**, (in press).

Wiin-Nielsen, A., Brown, John A., and Drake, Margaret, "Further Studies of Energy Exchange Between the Zonal Flow and the Eddies," *Tellus*, Vol. 16, No. 2, May **1964**, pp. 168–180.

CORRECTION NOTICE

Vol. 98, No. 4, Apr. 1970: p. 323, par. c, last line, 0.02 should be read instead of 0.20, and 0.001 instead of 0.01; p. 326, 2d par., lines 3 and 10, figure 3 should be read instead of figure 5.